

# The Conformational Flexibility of the Tetradentate Ligand <sup>t</sup>BuN4 is Essential for the Stabilization of (<sup>t</sup>BuN4)Pd<sup>III</sup> Complexes

Julia R. Khusnutdinova,<sup>†,§</sup> Nigam P. Rath,<sup>‡</sup> and Liviu M. Mirica<sup>\*,†</sup>

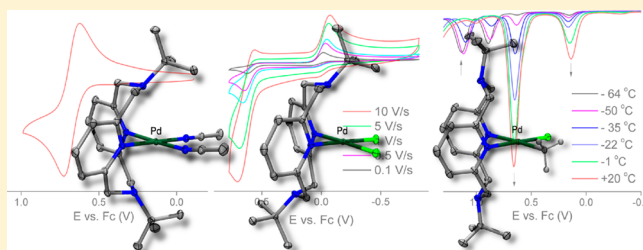
<sup>†</sup>Department of Chemistry, Washington University, One Brookings Drive, St. Louis, Missouri 63130-4899, United States

<sup>‡</sup>Department of Chemistry and Biochemistry, University of Missouri, One University Boulevard, St. Louis, Missouri 63121-4400, United States

## Supporting Information

**ABSTRACT:** The conformationally flexible tetradentate pyridinophane ligand <sup>t</sup>BuN4 effectively lowers the oxidation potential of (<sup>t</sup>BuN4)Pd<sup>II</sup> complexes and promotes their facile chemical and electrochemical oxidation, including unprecedented aerobic oxidation reactivity. While the low potential of a number of Pd<sup>II</sup> (and Pt<sup>II</sup>) complexes supported by various *fac*-chelating polydentate ligands is often attributed to the presence of a coordinating group in the axial position of the metal center, no detailed electrochemical studies have been reported for such systems. Described herein is the detailed

electrochemical investigation of the effect of ligand conformation on the redox properties of the corresponding Pd<sup>II</sup> complexes. These Pd complexes adopt different conformations in solution, as supported by studies using variable scan rate, variable-temperature cyclic voltammetry (CV), differential pulse voltammetry, and digital CV simulations at variable scan rates. The effect of the axial amine protonation on the spectroscopic and electrochemical properties of the complexes was also investigated. A number of new Pd<sup>III</sup> complexes were characterized by electron paramagnetic resonance, UV–vis spectroscopy, and X-ray diffraction including [(<sup>t</sup>BuN4)Pd<sup>III</sup>Cl<sub>2</sub>](ClO<sub>4</sub>), a dicationic [(<sup>t</sup>BuN4)Pd<sup>III</sup>Me(MeCN)](OTf)<sub>2</sub>, and an unstable tricationic [(<sup>t</sup>BuN4)Pd<sup>III</sup>(EtCN)<sub>2</sub>]<sup>3+</sup> species. Although the electron-rich neutral complexes (<sup>t</sup>BuN4)PdMeCl and (<sup>t</sup>BuN4)PdMe<sub>2</sub> are present in solution as a single isomer with the axial amines not interacting with the metal center, their low oxidation potentials are due to the presence of a minor conformer in which the <sup>t</sup>BuN4 ligand adopts a tridentate ( $\kappa^3$ ) conformation. In addition, the redox properties of the (<sup>t</sup>BuN4)Pd complexes show a significant temperature dependence, as the low-temperature behavior is mainly due to the contribution from the major, most stable conformer, while the room-temperature redox properties are due to the formation of the minor, more easily oxidized conformer(s) with the <sup>t</sup>BuN4 ligand acting as a tridentate ( $\kappa^3$ ) or tetradentate ( $\kappa^4$ ) ligand. Overall, the coordination to the metal center of each axial amine donor of the <sup>t</sup>BuN4 ligand leads to a lowering of the Pd<sup>II/III</sup> oxidation potential by ~0.6 V. These detailed electrochemical studies can thus provide important insights into the design of new ligands that can promote Pd-catalyzed oxidation reactions employing mild oxidants such as O<sub>2</sub>.



## INTRODUCTION

The Pd-catalyzed oxidation of C–H bonds is a rapidly developing field in transition metal catalysis that led to important practical applications in organic synthesis.<sup>1–8</sup> Various types of Pd-catalyzed C–H bond functionalization reactions to form new C–X bonds (X = OAc, OH, halide, NR<sub>2</sub>, etc.) have been developed.<sup>3,5–10</sup> These transformations are generally proposed to occur via a Pd-mediated C–H bond activation and oxidation to generate high-valent Pd<sup>III</sup> or Pd<sup>IV</sup> intermediates, followed by reductive elimination of a C–X bond.<sup>7,10,11</sup> However, a potential drawback of several of these transformations is the use of strong oxidants (e.g., hypervalent iodine or electrophilic fluorinating agents) needed to generate the high-valent Pd<sup>III</sup> or Pd<sup>IV</sup> species.<sup>3–8,12</sup> Similar limitations exist for other C–H functionalization reactions such as the Pt-catalyzed methane-to-methanol conversion in the Shilov system that requires the use of an expensive Pt<sup>IV</sup> oxidant to generate Pt<sup>IV</sup> intermediates responsible for MeOH formation.<sup>13,14</sup> In this

context, the search for more practical systems that can utilize mild oxidants—ideally air or O<sub>2</sub>—is an important challenge, and detailed electrochemical studies of high-valent organometallic complexes are essential for systematically determining what ligand systems and experimental conditions are needed for promoting facile catalytic oxidative reactions.

Several previous reports have suggested that the use of redox mediators or new ligand systems or additives can help achieve the desired oxidation transformations.<sup>5,15–19</sup> The use of polydentate ligands that control the redox properties of a metal center is one important approach that has been employed to design novel stoichiometric and catalytic systems for oxidation reactions using mild oxidants such as O<sub>2</sub>.<sup>20,21</sup> For example, the ability of tridentate *fac*-chelating ligands to promote the facile oxidation of Pd<sup>2+</sup><sup>22–27</sup> and Pt<sup>2+</sup><sup>28–33</sup> complexes

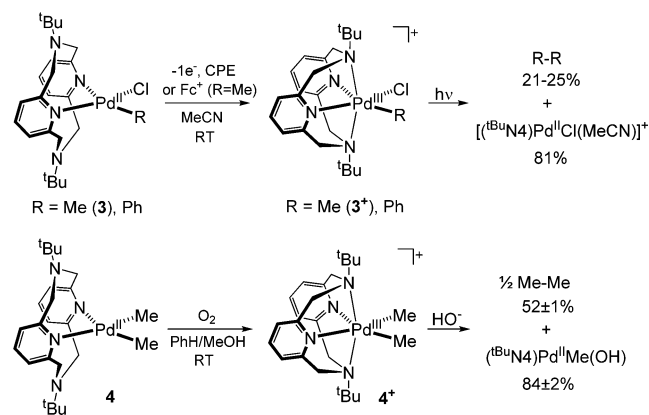
Received: September 24, 2014

Published: November 26, 2014

has been reported previously. The Pd<sup>II</sup> complexes of 1,4,7-trithiacyclononane (ttn), 1,4,7-triazacyclononane (tacn), and analogous N- and S-donor macrocyclic ligands can easily be oxidized to generate isolable Pd<sup>III</sup> coordination complexes,<sup>34–40</sup> while Pt complexes of tacn, *cis,cis*-1,3,5-triaminocyclohexane, or di-2-pyridylmethanesulfonate ligands are known to easily react with O<sub>2</sub> to produce Pt<sup>IV</sup> species.<sup>28–33</sup> Such facile oxidation was attributed to the interaction between the filled d<sub>z<sup>2</sup></sub> orbital of the metal center and the lone pair of an axial donor, which raises the energy of the d<sub>z<sup>2</sup></sub>-based highest occupied molecular orbital (HOMO) and thus lowers the Pd<sup>II</sup>/Pd<sup>III</sup> oxidation potential.<sup>29,41</sup> However, to the best of our knowledge no systematic electrochemical studies have been reported for either Pd or analogous Pt organometallic systems, despite the large number of Pd-catalyzed organic reactions. Such studies can help elucidate the mechanism and the effect of the axial donor coordination on the redox properties of the Pd center. In addition, Pd-catalyzed C–H functionalization reactions involving single-electron transfer (SET) steps and Pd<sup>III</sup> intermediates have been reported recently,<sup>42,43</sup> although the redox properties of such high-valent Pd species have not been investigated in detail.

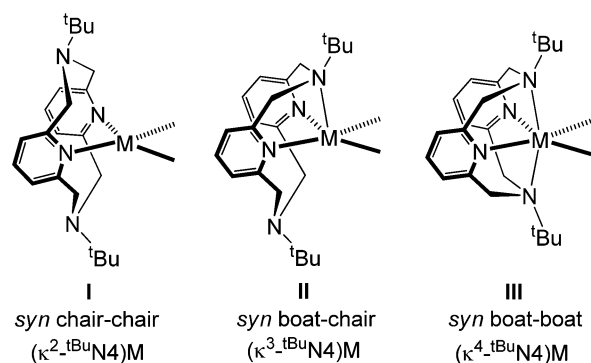
We have previously reported a class of tetradentate pyridinophane ligands <sup>R</sup>N4 (<sup>R</sup>N4 = N,N'-dialkyl-2,11-diaza-[3.3](2,6)pyridinophane; R = <sup>t</sup>Bu, <sup>i</sup>Pr, Me) that can stabilize Pd<sup>II</sup>, Pd<sup>III</sup>, and Pd<sup>IV</sup> oxidation states.<sup>44–49</sup> For example, a series of stable organometallic (<sup>t</sup>BuN4)Pd<sup>III</sup>RY<sup>+</sup> (R = Y = Me; R = Me, Y = Cl; R = Ph, Y = Cl) complexes were isolated and characterized for the first time in 2010.<sup>44</sup> The complexes [(<sup>t</sup>BuN4)Pd<sup>III</sup>Me<sub>2</sub>]<sup>+</sup> and [(<sup>t</sup>BuN4)Pd<sup>III</sup>MeCl]<sup>+</sup> were obtained by chemical oxidation with mild oxidants such as ferrocenium (Fc<sup>+</sup>) or even O<sub>2</sub>, or by electrochemical oxidation at relatively low potentials.<sup>44,45</sup> Moreover, these complexes exhibit photochemically or oxidatively induced C–C bond formation reactivity (Scheme 1), relevant to the oxidative coupling of C–H bond under mild oxidative conditions.<sup>44,45</sup>

**Scheme 1. Generation of (<sup>t</sup>BuN4)Pd<sup>III</sup>–Methyl Complexes and Their C–C Bond Formation Reactivity**



We have suggested that the unique ability of the <sup>t</sup>BuN4 ligand to stabilize the Pd<sup>III</sup> oxidation state is likely due to the ligand's conformational flexibility and the ability to adopt various coordination modes and act as a bidentate, tridentate, or tetradentate ligand (Scheme 2).<sup>44–49</sup> For instance, complexes (<sup>t</sup>BuN4)PdMe<sub>2</sub> and (<sup>t</sup>BuN4)PdMeCl exist as a single isomer in solution with <sup>t</sup>BuN4 binding to the Pd center through the two pyridyl N atoms, while the axial amines point away from the

**Scheme 2. Conformations of the <sup>t</sup>BuN4 Ligand in Transition Metal Complexes**



metal center. However, the oxidation potentials of (<sup>t</sup>BuN4)PdMe<sub>2</sub> and (<sup>t</sup>BuN4)PdMeCl are much lower compared to the analogous complexes with simple N-donor bidentate ligands such as 4,4'-di-*tert*-butyl-2,2'-bipyridine (<sup>t</sup>Bu<sub>2</sub>bipy).<sup>44,45,50</sup> This prompted us to investigate the effect of the ligand conformational flexibility on the redox properties and stability of Pd complexes in three oxidation states (+2, +3, and +4) and whether the precoordination of the amine donor(s) is essential for the facile oxidation reactivity of these complexes.

Cyclic voltammetry (CV), differential pulse voltammetry (DPV), and spectroelectrochemical studies, as well as CV digital simulations, were performed for a series of (<sup>t</sup>BuN4)Pd complexes that adopt various conformational states in solution ranging from (<sup>kappa</sup>2-<sup>t</sup>BuN4)Pd to (<sup>kappa</sup>3-<sup>t</sup>BuN4)Pd and (<sup>kappa</sup>4-<sup>t</sup>BuN4)Pd. Herein we have established that the facile oxidation reactivity of (<sup>t</sup>BuN4)PdMeCl and (<sup>t</sup>BuN4)PdMe<sub>2</sub> complexes is likely due to the presence in solution of a minor isomer with a tridentate or tetradentate <sup>t</sup>BuN4 ligand, which leads to a much lower oxidation potential for the corresponding Pd<sup>II</sup> complex. This is supported by temperature-dependent electrochemical studies that show temperature plays an important role in determining the redox behavior of these systems. In addition, the ligand conformational flexibility was also key in determining the redox properties of other Pd complexes such as (<sup>t</sup>BuN4)PdCl<sub>2</sub>, [(<sup>t</sup>BuN4)PdMe(MeCN)](OTf), and (<sup>t</sup>BuN4)Pd(RCN)<sub>2</sub>-(OTf)<sub>2</sub> (R = Me or Et). Overall, these results shed light on the role of conformational flexibility of the ligand and reveals the profound effect of the axial amine coordination on the oxidation potentials of the corresponding Pd complexes and formation of high-valent Pd species. Understanding the factors that determine the redox behavior of organometallic Pd complexes is of great importance to the field of transition metal catalysis as it can provide insight into the design of novel ligands that promote Pd-catalyzed oxidation reactions using mild oxidants such as O<sub>2</sub>.

## EXPERIMENTAL DETAILS

**General Specifications.** All manipulations were performed under a nitrogen atmosphere using standard Schlenk and glovebox techniques if not indicated otherwise. All reagents for which synthesis is not given were commercially available from Sigma-Aldrich, Acros, Strem, or Pressure Chemical and were used as received without further purification. Solvents were purified prior to use by passing through a column of activated alumina using an MBRAUN SPS. <sup>t</sup>BuN4,<sup>51</sup> (<sup>t</sup>BuN4)Pd<sup>II</sup>Cl<sub>2</sub> (2),<sup>52</sup> [(<sup>t</sup>BuN4)Pd<sup>II</sup>Me(MeCN)](OTf) (3<sup>+</sup>[OTf]),<sup>45</sup> (<sup>t</sup>BuN4)Pd<sup>II</sup>MeCl (4),<sup>52</sup> [(<sup>t</sup>BuN4)Pd<sup>III</sup>MeCl](BF<sub>4</sub>),<sup>44</sup> (<sup>t</sup>BuN4)-Pd<sup>III</sup>Me<sub>2</sub>,<sup>44,45</sup> (<sup>t</sup>Bu<sub>2</sub>bipy)Pd<sup>II</sup>MeCl,<sup>53</sup> and (tmeda)Pd<sup>III</sup>MeCl<sup>54</sup> were prepared according to the literature procedures. <sup>1</sup>H (300 MHz) and

$^{13}\text{C}$  NMR spectra were recorded on a Varian Mercury-300 spectrometer. Chemical shifts are reported versus tetramethylsilane and are referenced to residual solvent resonance peaks.<sup>55</sup> Abbreviations for the multiplicity of NMR signals are s (singlet), d (doublet), t (triplet), q (quartet), m (multiplet), br (broad). UV–visible spectra were recorded on a Varian Cary 50 Bio spectrophotometer and are reported as  $\lambda_{\text{max}}$  nm ( $\epsilon$ ,  $\text{M}^{-1}\cdot\text{cm}^{-1}$ ). Electron paramagnetic resonance (EPR) spectra were recorded on a JEOL JES-FA X-band (9.2 GHz) EPR spectrometer at 77 K. The EPR spectra were simulated with the WinEPR SimFonia (v.1.25) program. Electrospray ionization mass spectrometry (ESI-MS) experiments were performed using a Bruker Maxis QTOF mass spectrometer with an ESI source. ESI MS was provided by the Washington University Mass Spectrometry Resource, an NIH Research Resource (Grant No. P41RR0954). Elemental analyses were carried out by the Columbia Analytical Services Tucson Laboratory.

**Electrochemical Measurements.** The CV experiments were performed with a BASi EC Epsilon electrochemical workstation or a CHI 660D Electrochemical Analyzer. Electrochemical-grade  $\text{Bu}_4\text{NClO}_4$ ,  $\text{Bu}_4\text{NBF}_4$ , or  $\text{Bu}_4\text{NPF}_6$  (Fluka) were used as the supporting electrolytes. Electrochemical measurements were performed under a blanket of nitrogen, and the analyzed solutions were deaerated by purging with nitrogen or prepared in degassed solvents in the glovebox. A glassy carbon disk electrode ( $d = 1.6$  mm or 1.0 mm) or a platinum disk electrode ( $d = 1.6$  mm) were used as the working electrode. For room-temperature measurements, a nonaqueous  $\text{Ag}/0.01$  M  $\text{AgNO}_3/\text{MeCN}$  reference electrode was used. For low-temperature studies, a Ag wire pseudoreference electrode was employed. The reference electrodes were calibrated against ferrocene (Fc) at each temperature. The glassy carbon working electrode was polished before each run using alumina (BASi). Preparative electrochemical oxidations were performed in a two-compartment bulk electrolysis cell equipped with a Teflon cap and a magnetic stirring bar; the auxiliary chamber was separated from the working compartment by a medium-frit glass junction. For controlled potential electrolysis the working electrode was a Pt gauze (Aldrich, 25 mm  $\times$  10 mm) or reticulated vitreous carbon (BASi), while the auxiliary electrode was a coiled Pt wire ( $d = 0.5$  mm, 23 cm) or a Pt gauze (Aldrich, 25 mm  $\times$  10 mm). Electrochemical oxidations were performed at a constant potential at 20 °C under a blanket of nitrogen in deaerated solutions. The CV and UV–vis spectra were recorded before and after electrolysis. The separations between the anodic and cathodic peaks in the CVs of ferrocene in 0.1 M  $\text{Bu}_4\text{NClO}_4$  solutions were as follows: 94 mV in MeCN, 119 mV in  $\text{CH}_2\text{Cl}_2$ , and 193 mV in tetrahydrofuran (THF) at 20 °C; no  $iR$  compensation was applied during these CVs.

**Digital CV Simulations.** The Electrochemical Simulation Package (ESP)<sup>56,57</sup> was used for digital simulation and nonlinear optimization of the model parameters against the experimental data. The digital simulations were compared with those performed using the “analog” waveform simulator CVSIM<sup>58,59</sup> with the same parameters to give almost identical results. For the CV simulations in ESP, the parameters  $E$  (redox potential),  $k_c$  (heterogeneous rate constant), and  $k_f$  and  $k_b$  (homogeneous chemical reaction rate constants for forward and reverse reactions, respectively) were optimized to fit the experimental data using the program-implemented procedure. The diffusion coefficients were not optimized and were approximated as  $1.0 \times 10^{-5}$   $\text{cm}^2/\text{s}$  for all species; the transfer coefficient  $\alpha$  was not optimized and was approximated as 0.5 for all redox couples. The values for the solution resistance and double-layer capacitance were adjusted manually, and the same values were used for all fits. The electrode area is 0.0201  $\text{cm}^2$ . The procedure was repeated for each scan rate separately, and the parameters that give satisfactory fits for all scan rates were selected and used for the simulations shown in Figures 7, 12, and 21. The open-circuit potentials were used as the initial potentials for the CV scans. The detailed description of the parameters used for simulations is given in the Supporting Information.

**Preparation of  $[(^{\text{tBu}}\text{N4})\text{Pd}^{\text{II}}(\text{MeCN})_2](\text{OTf})_2$  (1).** A solution of  $\text{AgOTf}$  (72.2 mg, 0.281 mmol) in MeCN (5 mL) was added to a stirred solution of  $(^{\text{tBu}}\text{N4})\text{Pd}^{\text{II}}\text{Cl}_2$  (74.5 mg, 0.141 mmol) in MeCN (15 mL). A white precipitate of  $\text{AgCl}$  appeared immediately, and the

color of the solution changed from orange-yellow to blue. The stirring was continued at room temperature (RT) overnight in the dark. The  $\text{AgCl}$  precipitate was filtered through Celite, the resulting blue solution was rotary evaporated, and the blue residue was redissolved in 2 mL of dry MeCN and filtered through Celite. The clear blue filtrate was layered with dry ether to give large blue crystals after several days at RT. The crystalline product was removed by filtration, washed with ether and pentane, and dried under vacuum. Yield 85.1 mg (0.101 mmol), 72%, blue crystalline solid. UV–vis,  $\lambda$ , nm ( $\epsilon$ ,  $\text{M}^{-1}\cdot\text{cm}^{-1}$ ), MeCN: 268 (8800), 353 (312), 613 (89).  $^1\text{H}$  NMR ( $\text{CD}_3\text{CN}$ , 25 °C, 300 MHz),  $\delta$ : 1.58 (s, 18H,  $^{\text{tBu}}$ ), 3.62 (d,  $J = 17.1$  Hz, 4H,  $\text{CH}_2$ ), 4.86 (d,  $J = 17.1$  Hz, 4H,  $\text{CH}_2$ ), 7.25 (d,  $J = 7.9$  Hz, 4H,  $\text{Py H}_{\text{meta}}$ ), 7.80 (t,  $J = 7.9$  Hz, 2H,  $\text{Py H}_{\text{para}}$ ). The  $\text{CH}_3\text{CN}$  ligand molecules exchange with  $\text{CD}_3\text{CN}$  in solution, and a peak of free acetonitrile appears as a singlet at 1.96 ppm upon dissolution of  $[(^{\text{tBu}}\text{N4})\text{Pd}(\text{CH}_3\text{CN})_2](\text{OTf})_2$  in  $\text{CD}_3\text{CN}$ . X-ray quality crystals were obtained by slow crystallization from MeCN by ether diffusion during the course of several weeks. Anal. Found: C, 40.41; H, 4.66; N, 10.06. Calcd for  $\text{C}_{28}\text{H}_{38}\text{F}_6\text{N}_6\text{O}_6\text{PdS}_2$ : C, 40.07; H, 4.56; N, 10.01%.

**Preparation of  $[(^{\text{tBu}}\text{N4-H}^+)\text{Pd}^{\text{II}}(\text{MeCN})_2](\text{OTf})_3$ , 1-HOTf.** Anhydrous triflic acid (HOTf, 3.4  $\mu\text{L}$ , 0.038 mmol) was added to a solution of  $[(^{\text{tBu}}\text{N4})\text{Pd}^{\text{II}}(\text{MeCN})_2](\text{OTf})_2$  (32.3 mg, 0.038 mmol) in 2 mL of MeCN. Upon addition of the acid, the initially blue solution of  $[(^{\text{tBu}}\text{N4})\text{Pd}^{\text{II}}(\text{MeCN})_2](\text{OTf})_2$  immediately changed color to pink. The solution was rotary evaporated to dryness, triturated with ether to give a pink crystalline material that was washed with ether and pentane, and air-dried. The NMR of the product obtained from the reaction with 1 equiv of  $\text{HBF}_4$  is identical to that obtained when 1 equiv of HOTf was used.  $^1\text{H}$  NMR ( $\text{CD}_3\text{CN}$ , 25 °C, 300 MHz),  $\delta$ : 1.60 (s, 9H,  $^{\text{tBu}}$ ), 1.75 (s, 9H,  $^{\text{tBu}}$ ), 3.96 (d,  $J = 17.6$ , 2H,  $\text{CH}_2$ ), 5.03 (d,  $J = 17.6$  Hz, 2H,  $\text{CH}_2$ ), 5.94 (d,  $J = 15.7$  Hz, 2H,  $\text{CH}_2$ ), 6.69 (dd,  $J = 15.7$ , 5.4 Hz, 2H,  $\text{CH}_2$ ), 7.56 (d,  $J = 7.8$  Hz, 2H,  $\text{Py H}_{\text{meta}}$ ), 7.67 (d,  $J = 7.8$  Hz, 2H,  $\text{Py H}_{\text{meta}}$ ), 8.01 (vt,  $J = 7.8$  Hz, 2H,  $\text{Py H}_{\text{para}}$ ), 8.13 (br s, 1H, NH). The  $\text{CH}_3\text{CN}$  ligand molecules exchange with  $\text{CD}_3\text{CN}$  in solution, and a peak of free acetonitrile appears as a singlet at 1.96 ppm. X-ray quality crystals were obtained by diffusion of ether into a MeCN solution at  $-20$  °C. Elemental analysis of the isolated sample of  $[(^{\text{tBu}}\text{N4-H}^+)\text{Pd}(\text{MeCN})_2](\text{OTf})_3$  failed to produce consistent results likely due to loss of HOTf during sample storage (Anal. Found: C, 33.61; H, 4.52; N, 7.73; Calcd for  $\text{C}_{29}\text{H}_{39}\text{F}_9\text{N}_6\text{O}_6\text{PdS}_3$ : C, 35.21; H, 3.97; N, 8.50%). UV–vis (MeCN)  $\lambda$ , nm ( $\epsilon$ ,  $\text{M}^{-1}\cdot\text{cm}^{-1}$ ): 265 (14 200),  $\sim$ 326 (sh, 370), 498 (116).

**Preparation of  $[(^{\text{tBu}}\text{N4})\text{Pd}^{\text{III}}\text{Cl}_2](\text{ClO}_4)_2$  ( $2^+[\text{ClO}_4]$ ).** A solution of  $(^{\text{tBu}}\text{N4})\text{PdCl}_2$  (971 mg, 1.83 mmol) in 65 mL of 0.1 M  $\text{Bu}_4\text{NClO}_4/\text{CH}_2\text{Cl}_2$  was placed into a 100 mL bulk electrolysis cell equipped with a magnetic stirring bar. Reticulated vitreous carbon was used as the working electrode, and  $\text{Ag}/0.01$  M  $\text{AgNO}_3/\text{MeCN}$  was used as the reference electrode. A platinum coil was used as the auxiliary electrode and was separated from the working chamber by a glass frit. The solution was degassed by bubbling with  $\text{N}_2$  for 15 min. Electrolysis was performed at 1 V versus  $\text{Ag}/\text{AgNO}_3/\text{MeCN}$  in a stirred solution under a blanket of  $\text{N}_2$ . When a charge corresponding to a  $1e^-$  oxidation passed, the current dropped, and the electrolysis was stopped. During electrolysis, the yellow-orange solution darkened, and a green solid precipitated. After electrolysis, the resulting suspension was stored at  $-20$  °C overnight. The green precipitate was removed by filtration, washed with cold  $\text{CH}_2\text{Cl}_2$ , ether and pentane, and dried under vacuum. Yield: 903 mg of green solid, 78%. The product was recrystallized by diffusion of ether into a saturated MeCN solution at RT to give green crystals of  $[(^{\text{tBu}}\text{N4})\text{Pd}^{\text{III}}\text{Cl}_2]\text{ClO}_4\cdot\text{MeCN}$ . X-ray quality crystals were obtained by diffusion of ether into a MeCN solution at RT. Evans method ( $\text{CD}_3\text{CN}$ ):  $\mu_{\text{eff}} = 1.62 \mu_{\text{B}}$ . UV–vis,  $\lambda$ , nm ( $\epsilon$ ,  $\text{M}^{-1}\cdot\text{cm}^{-1}$ ), MeCN: 260 (18 500), 399 (3290), 723 (2420). Anal. Found: C, 43.03; H, 5.34; N, 10.33. Calcd for  $[(^{\text{tBu}}\text{N4})\text{Pd}^{\text{III}}\text{Cl}_2]\cdot\text{ClO}_4\cdot\text{MeCN}$ ,  $\text{C}_{24}\text{H}_{35}\text{Cl}_3\text{N}_5\text{O}_4\text{Pd}$ : C, 43.00; H, 5.26; N, 10.45%.

**General Procedure for Low-Temperature Electrolysis and Spectroelectrochemical Studies.** Spectroelectrochemical oxidations were performed in a custom-built two-compartment electrolysis cell consisting of a working chamber containing a Hellma fiber-optic immersion probe (1 mm path length) and equipped with a magnetic

stirring bar and an auxiliary chamber separated with a fine-porosity frit junction. The working chamber was also equipped with a reticulated vitreous carbon electrode placed in close proximity to the immersion probe, the working CV electrode (Pt disk,  $d = 1$  mm), and the Ag wire pseudoreference electrode. A coiled Pt wire was used as the auxiliary electrode. Cyclic voltammograms were recorded at  $-65$  °C before the electrolysis, and the applied potential was typically chosen to be 200–250 mV more positive than the peak potential of the oxidation wave of interest. The electrolysis was performed at  $-65$  °C in a stirred solution at a constant potential under a flow of nitrogen. During the electrolysis, the UV–vis spectra were recorded every 0.3 min using a Varian Cary 50 Bio spectrophotometer and the Scanning Kinetics program. After electrolysis, aliquots were transferred to precooled quartz EPR tubes, frozen, and stored in liquid  $N_2$  for EPR characterization.

**X-ray Structure Determination of 1, 1·HOTf,  $\kappa^3$ -2, 2 $^+$ [ClO $_4$ ], 3 $^+$ [OTf] $_2$ , and 4.** Suitable crystals of appropriate dimensions were mounted on Mitgen loops in random orientations. Preliminary examination and data collection were performed using a Bruker Kappa Apex-II charge coupled device (CCD) detector system or a Bruker SMART Apex-II single-crystal X-ray diffractometer equipped with an Oxford Cryostream LT device. Data were collected using graphite monochromated Mo  $K\alpha$  radiation ( $\lambda = 0.71073$  Å) from a fine focus sealed tube X-ray source. Preliminary unit cell constants were determined with a set of 36 narrow frame scans. Typical data sets consist of a combination of  $\omega$  and  $\phi$  scan frames with typical scan width of  $0.5^\circ$  and counting time of 15–30 s/frame at a crystal to detector distance of  $\sim 4.0$  cm. The collected frames were integrated using an orientation matrix determined from the narrow frame scans. Apex II and SAINT software packages<sup>60</sup> were used for data collection and data integration. Analysis of the integrated data did not show any decay. Final cell constants were determined by global refinement of reflections from the complete data set. Data were corrected for systematic errors using SADABS<sup>60</sup> based on the Laue symmetry using equivalent reflections. Crystal data and intensity data collection parameters are listed in Tables S2–S15 in the Supporting Information. Structure solutions and refinement were carried out using the SHELXTL-PLUS software package.<sup>61</sup> The structures were solved by direct methods in space groups listed below. The structures were refined with full matrix least-squares refinement by minimizing  $\sum w(F_o^2 - F_c^2)^2$ . All non-hydrogen atoms were refined anisotropically to convergence. All H atoms were added in the calculated position and were refined using appropriate riding models (AFIX m3).

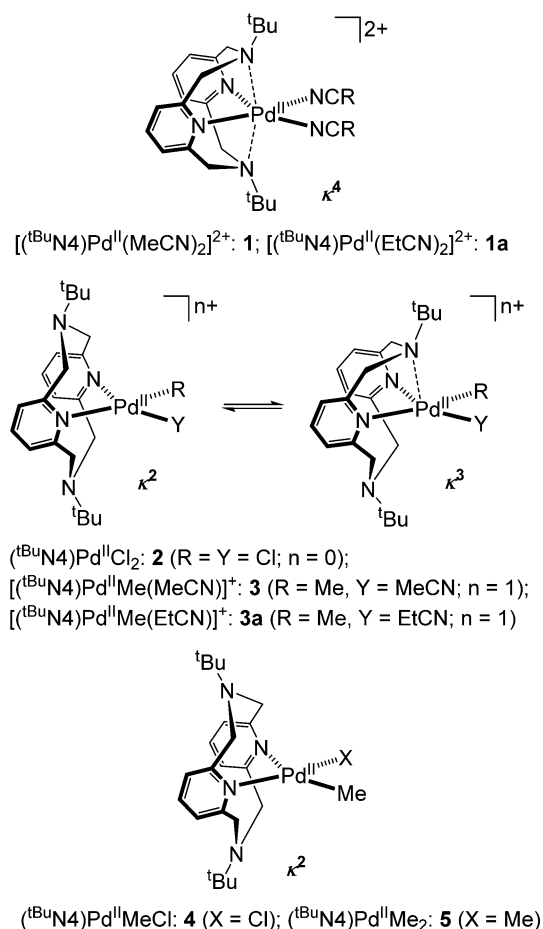
## RESULTS AND DISCUSSION

### Conformational Equilibria in $(t^{\text{Bu}}\text{N}_4)\text{Pd}$ Complexes.

The  $t^{\text{Bu}}\text{N}_4$  ligand and its analogues are known to adopt mainly three conformations in transition metal complexes (I–III, Scheme 2). In the electron-rich neutral Pd complexes such as  $(^R\text{N}_4)\text{Pd}^{\text{II}}\text{Me}_2$  and  $(^R\text{N}_4)\text{Pd}^{\text{II}}\text{MeCl}$  ( $R = t^{\text{Bu}}, t^{\text{Pr}}, \text{Me}$ ), the  $^R\text{N}_4$  ligand adopts the *syn* chair–chair conformation I, both in solution and in the solid state (Chart 1).<sup>44,45,47,52</sup> The  $^R\text{N}_4$  ligand coordinates to the square planar  $\text{Pd}^{\text{II}}$  center through the two pyridyl N atoms, while the lone pairs of the amine groups point away from the metal center and are not interacting with the Pd center. The chair–chair conformation was also reported for the free  $t^{\text{Bu}}\text{N}_4$  ligand in the solid state.<sup>51</sup> In addition, the  $^R\text{N}_4$  ligand can bind in a tetradentate fashion to the metal center through all four N atoms by adopting the *syn* boat–boat conformation III (Scheme 2). This conformation is common for first row transition metal complexes<sup>51,62–67</sup> and high-valent  $\text{Pd}^{\text{III}}$  and  $\text{Pd}^{\text{IV}}$  complexes.<sup>44,47</sup> The only example of a  $(^R\text{N}_4)\text{Pd}^{\text{II}}$  complex exhibiting conformation III is reported herein for the dicationic species  $[(t^{\text{Bu}}\text{N}_4)\text{Pd}^{\text{II}}(\text{MeCN})_2](\text{OTf})_2$  (Chart 1).

Kress and co-workers reported variable-temperature NMR studies of the conformational equilibria for the  $(t^{\text{Bu}}\text{N}_4)\text{Pd}^{\text{II}}\text{Cl}_2$  and  $[(t^{\text{Bu}}\text{N}_4)\text{Pd}^{\text{II}}\text{Me}(\text{MeCN})]^+$  complexes and showed that

**Chart 1.**  $(t^{\text{Bu}}\text{N}_4)\text{Pd}$  Complexes Employed in This Study, Shown in Their Most Stable Conformations

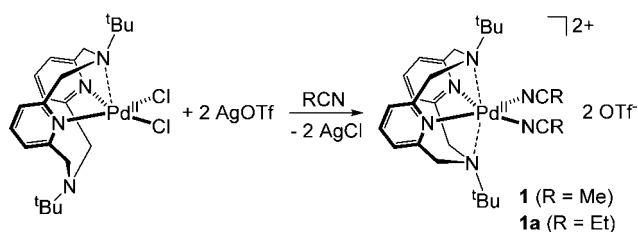


they exist in solution as a mixture of two interconverting isomers with the  $t^{\text{Bu}}\text{N}_4$  ligand coordinated in a bidentate or a tridentate fashion and adopting a *syn* chair–chair or a *syn* boat–chair conformation, respectively (I and II in Chart 1).<sup>52</sup> This conformational assignment was confirmed by nuclear Overhauser effect (NOE) NMR studies.<sup>52</sup>

Herein we have explored the effect of the conformational flexibility of the  $t^{\text{Bu}}\text{N}_4$  ligand on the electrochemical properties of a series of  $\text{Pd}^{\text{II}}$  complexes that exhibit different conformations in solution (Chart 1):  $[(\kappa^4\text{-}t^{\text{Bu}}\text{N}_4)\text{Pd}^{\text{II}}(\text{RCN})_2]^{2+}$  ( $R = \text{Me}, \text{Et}$ );  $(t^{\text{Bu}}\text{N}_4)\text{Pd}^{\text{II}}\text{Cl}_2$ , and  $[(t^{\text{Bu}}\text{N}_4)\text{Pd}^{\text{II}}\text{Me}(\text{MeCN})]^+$ , which are present as a mixture of  $\kappa^2$ - and  $\kappa^3$ -isomers; and  $(\kappa^2\text{-}t^{\text{Bu}}\text{N}_4)\text{Pd}^{\text{II}}\text{MeCl}$  and  $(\kappa^2\text{-}t^{\text{Bu}}\text{N}_4)\text{Pd}^{\text{II}}\text{Me}_2$ . We first discuss the  $[(\kappa^4\text{-}t^{\text{Bu}}\text{N}_4)\text{Pd}^{\text{II}}(\text{RCN})_2]^{2+}$  complexes as they exhibit a simple electrochemical behavior and thus facilitate the discussion of the other Pd complexes with more complex redox properties.

**Characterization and Electrochemical Behavior of  $[(t^{\text{Bu}}\text{N}_4)\text{Pd}^{\text{II}}(\text{RCN})_2](\text{OTf})_2$  ( $R = \text{Me}, \text{Et}$ ).** The complex  $[(t^{\text{Bu}}\text{N}_4)\text{Pd}^{\text{II}}(\text{MeCN})_2](\text{OTf})_2$ , **1**, was synthesized by reacting  $(t^{\text{Bu}}\text{N}_4)\text{PdCl}_2$  with 2 equiv of  $\text{AgOTf}$  in MeCN (Scheme 3). The complex **1** was isolated in 72% yield as a blue crystalline solid and characterized by NMR, elemental analysis, and single-crystal X-ray diffraction. Alternatively, the analogous complex with a  $\text{BF}_4^-$  counteranion can be prepared by the reaction of  $[(\text{MeCN})_4\text{Pd}](\text{BF}_4)_2$  with  $t^{\text{Bu}}\text{N}_4$ , although this reaction is less clean due to the formation of monoprotonated ligand  $t^{\text{Bu}}\text{N}_4\text{-H}^+$ . The  $^1\text{H}$  NMR of  $[(t^{\text{Bu}}\text{N}_4)\text{Pd}^{\text{II}}(\text{MeCN})_2](\text{OTf})_2$  is

**Scheme 3. Synthesis of  $[(\text{t}^{\text{Bu}}\text{N}4)\text{Pd}^{\text{II}}(\text{RCN})_2](\text{OTf})_2$  ( $\text{R} = \text{Me}, \text{Et}$ )**



indicative of a  $C_{2v}$  symmetric structure in solution. The signal of the *t*-butyl group appears as a singlet at 1.58 ppm, typical for  $(\text{t}^{\text{Bu}}\text{N}4)\text{Pd}$  complexes with the  $^t\text{Bu}$  group pointing toward the Pd center (typically 1.40–1.64 ppm), and shifted downfield compared to the chemical shift of the  $^t\text{Bu}$  groups pointing away from the Pd center (typically 1.24–1.34 ppm).<sup>52</sup> The 3.62 ppm chemical shift of one of the doublets for the  $\text{CH}_2$  groups is also characteristic for  $(\text{t}^{\text{Bu}}\text{N}4)\text{Pd}$  complexes with an amine group coordinated to Pd and is attributed to the shielding effect of the pyridine rings in these conformations.<sup>52</sup> Single crystals of **1** were obtained by slow diffusion of diethyl ether into a MeCN solution for several days. The X-ray analysis reveals that the  $\text{t}^{\text{Bu}}\text{N}4$  ligand adopts the *syn* boat–boat conformation **III** with the two pyridyl N atoms bound to Pd and the two amine donors present in close proximity to the metal center, with Pd– $\text{N}_{\text{amine}}$  distances of 2.594 and 2.603 Å (Figure 1a). The close

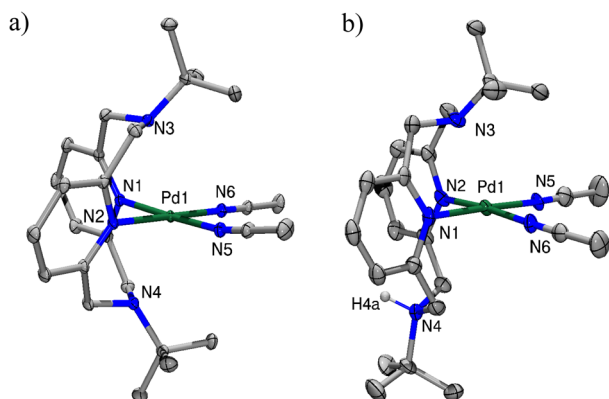


**Figure 1.** ORTEP representation (50% probability ellipsoids) of the cation of  $[(\text{t}^{\text{Bu}}\text{N}4)\text{Pd}^{\text{II}}(\text{MeCN})_2](\text{OTf})_2$ , **1** (a) and the cation of  $[(\text{t}^{\text{Bu}}\text{N}4\text{-H}^+)\text{Pd}^{\text{II}}(\text{MeCN})_2](\text{OTf})_3 \cdot 1 \cdot \text{HOTf}$  (b). Selected bond lengths (Å), (a): Pd1–N1 2.023(1); Pd1–N2 2.005(1); Pd1–N3 2.594(1); Pd1–N4 2.603(1); Pd1–N5 2.017(1); Pd1–N6 2.003(1). (b): Pd1–N1 2.010(7); Pd1–N2 1.999(7); Pd1–N3 2.525(7); Pd1–N5 1.987(7); Pd1–N6 1.995(7).

proximity of amine N donors to the Pd center is likely due to an electrostatic interaction between the amine N lone pairs and the dicationic  $\text{Pd}^{\text{II}}$  center. Interestingly, **1** is characterized by a weak absorption band in the visible region at 613 nm ( $\epsilon = 89 \text{ M}^{-1} \text{ cm}^{-1}$ ) tentatively assigned as a d–d transition. The presence of a similar absorption band and blue color was observed previously for  $\text{Pd}^{\text{II}}$  complexes with axial N- or S-donor atoms in close proximity to the metal center.<sup>68–72</sup>

The bis-propionitrile complex  $[(\text{t}^{\text{Bu}}\text{N}4)\text{Pd}^{\text{II}}(\text{EtCN})_2](\text{OTf})_2$ , **1a**, was synthesized similarly using EtCN as the solvent (Scheme 3) and characterized by elemental analysis and X-ray diffraction. Although the crystal quality did not allow for a complete structure refinement, the observed atom connectivity

established was consistent with the  $\text{t}^{\text{Bu}}\text{N}4$  ligand adopting a tetradentate  $\kappa^4$  conformation, similar to that observed in **1**.<sup>73</sup>

The CV of **1** in  $\text{Bu}_4\text{NPF}_6/\text{MeCN}$  exhibits a quasireversible one-electron oxidation wave at  $E_{1/2} = 674 \text{ mV}$  versus ferrocene (Fc) with a separation between the forward and reverse peaks of  $\Delta E_p = 99 \text{ mV}$  (Figure 2). A similar CV was obtained for **1a**

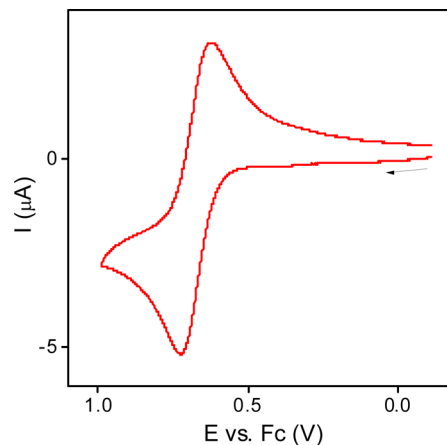


**Figure 2.** CV of 1.0 mM  $[(\text{t}^{\text{Bu}}\text{N}4)\text{Pd}^{\text{II}}(\text{MeCN})_2](\text{OTf})_2$  (**1**) in 0.5 M  $\text{Bu}_4\text{NPF}_6/\text{MeCN}$  (100 mV/s, RT).

in  $\text{Bu}_4\text{NBF}_4/\text{EtCN}$  with the quasireversible oxidation at  $E_{1/2} = 655 \text{ mV}$  versus Fc ( $\Delta E_p = 74 \text{ mV}$ , Figure S19).<sup>73</sup> The small separation between the forward and reverse peaks suggests that only a minor geometrical reorganization occurs upon oxidation of  $(\kappa^4\text{-t}^{\text{Bu}}\text{N}4)\text{Pd}^{\text{II}}$  to  $\text{Pd}^{\text{III}}$ .<sup>74,75</sup> Indeed, since in the previously reported  $(\text{t}^{\text{Bu}}\text{N}4)\text{Pd}^{\text{III}}$  complexes the  $\text{t}^{\text{Bu}}\text{N}4$  ligand was found to coordinate in a tetradentate fashion with the Pd– $\text{N}_{\text{amine}}$  distances in a range of 2.413–2.484 Å,<sup>44</sup> in **1** and **1a**  $\text{t}^{\text{Bu}}\text{N}4$  is expected to remain in the same *syn* boat–boat  $\kappa^4$  conformation upon oxidation to  $\text{Pd}^{\text{III}}$ .

To obtain the corresponding  $\text{Pd}^{\text{III}}$  product, controlled potential electrolysis (CPE) of  $[(\text{t}^{\text{Bu}}\text{N}4)\text{Pd}^{\text{II}}(\text{EtCN})_2](\text{OTf})_2$  was performed in EtCN at  $-65 \text{ }^\circ\text{C}$  by applying a potential 200 mV higher than the  $E_{1/2}$  of the  $\text{Pd}^{\text{II}}/\text{Pd}^{\text{III}}$  couple. The oxidation of **1a** was monitored by UV–vis and led to the formation of a dark-blue solution of a paramagnetic product assigned as  $[(\kappa^4\text{-N}4)\text{Pd}^{\text{III}}(\text{EtCN})_2]^{3+}$  and characterized by intense absorption bands at 615 nm ( $\epsilon = 5200 \text{ M}^{-1} \text{ cm}^{-1}$ ) and 354 nm ( $\epsilon = 1800 \text{ M}^{-1} \text{ cm}^{-1}$ , Figure 3). The product of one-electron oxidation was characterized by UV–vis and EPR spectroscopy at low temperature due to its limited stability at higher temperatures. The EPR spectrum (Figure 4) reveals an axial signal with  $g_x = g_y = 2.102$  and  $g_z = 2.000$  and superhyperfine coupling to the two axial N atoms ( $A_{\text{N},x} = A_{\text{N},y} = 17.0 \text{ G}$ ;  $A_{\text{N},z} = 25.5 \text{ G}$ ), consistent with the presence of a  $\text{Pd}^{\text{III}}$  center in a  $d_{5/2}$ -ground state with appreciable axial Pd– $\text{N}_{\text{amine}}$  interactions.<sup>44,45,47</sup>

The reversible oxidations of **1** and **1a** represent examples where the conformation of the ligand most likely does not change upon one-electron oxidation. Importantly, the absence of significant conformational changes in these complexes can also be implied from their quasireversible  $\text{Pd}^{\text{II}}/\text{Pd}^{\text{III}}$  redox waves with a small peak-to-peak separation, as observed in the CV scans. This is in contrast to the  $\text{Pd}^{\text{II}}/\text{Pd}^{\text{III}}$  redox waves with large peak-to-peak separation for the Pd complexes that undergo a large conformational change upon oxidation (see below).

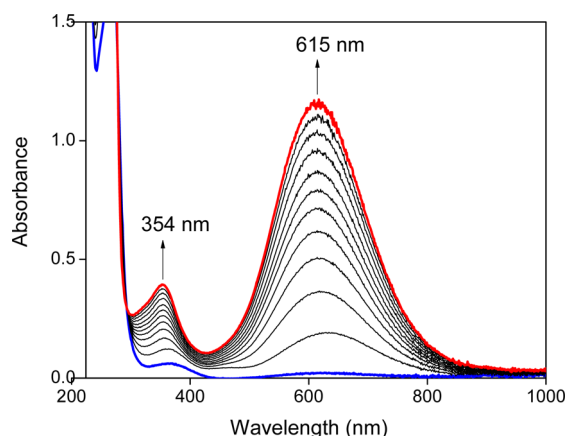


**Figure 3.** UV-vis spectra of CPE of 2.2 mM  $[(t^{\text{Bu}}\text{N}_4)\text{Pd}^{\text{II}}(\text{EtCN})_2](\text{OTf})_2$  in 0.1 M  $\text{Bu}_4\text{NClO}_4/\text{EtCN}$  (1 mm path length,  $-65^\circ\text{C}$ ,  $\Delta t = 18$  min). Arrows indicate the change of the absorption intensity over time.

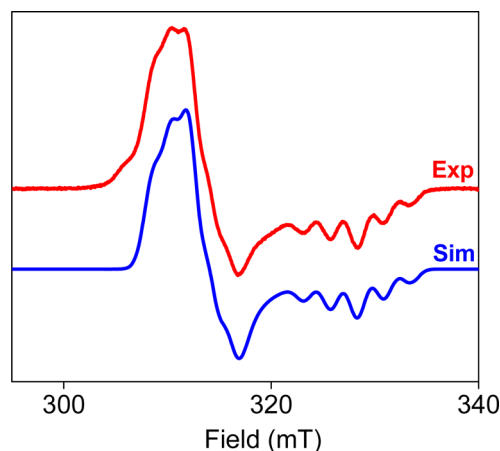


**Figure 4.** EPR spectrum of  $[(t^{\text{Bu}}\text{N}_4)\text{Pd}^{\text{III}}(\text{EtCN})_2]^{3+}$  in EtCN, 77K (red) and simulated spectrum (blue). The parameters used for the simulation were  $g_x = g_y = 2.102$  ( $A_{N_x} = A_{N_y} = 17.0$  G),  $g_z = 2.000$  ( $A_{N_z} = 25.5$  G).

Interestingly, the protonation of one of the amine arms of  $t^{\text{Bu}}\text{N}_4$  with 1 equiv of a strong acid such as HOTf or  $\text{HBF}_4$  leads to the formation of a complex in which  $t^{\text{Bu}}\text{N}_4$  adopts a *syn* boat-chair conformation and binds in a tridentate fashion to the Pd center through two pyridyl and one amine N atoms, while the protonated amine points away from the Pd. The complex obtained by the reaction of  $[(t^{\text{Bu}}\text{N}_4)\text{Pd}^{\text{II}}(\text{MeCN})_2](\text{OTf})_2$  with 1 equiv HOTf was isolated as a pink crystalline solid and characterized by X-ray diffraction and NMR as a tricationic complex  $[(t^{\text{Bu}}\text{N}_4\text{-H}^+)\text{Pd}^{\text{II}}(\text{MeCN})_2](\text{OTf})_3$ , **1**-HOTf (Figure 1b). The configuration of the protonated amine is such that the hydrogen atom of the N–H group points away from the Pd center. This is likely due to steric reasons as such a configuration avoids the repulsion between the *t*Bu group of the protonated amine and the pyridyl rings. Therefore, while the ability of the amine N atoms of  $t^{\text{Bu}}\text{N}_4$  to act as a “proton shuttle” may be inhibited by this unfavorable configuration,  $t^{\text{Bu}}\text{N}_4$  analogs with less bulky N-substituents may be more suitable for promoting such proton-shuttling reactivity.<sup>76–78</sup>

The NMR of **1**-HOTf in MeCN reveals the presence of an NH proton as a broad singlet at 8.13 ppm and a  $C_s$  symmetry of the complex in solution. The weak absorption band of **1**

tentatively assigned as a d-d transition shifts hypsochromically upon protonation to 498 nm ( $\epsilon = 116 \text{ M}^{-1} \text{ cm}^{-1}$ ). In addition, the CV of **1**-HOTf exhibits two irreversible oxidation waves at much higher potentials, 1.45 and 1.64 V vs Fc (Supporting Information, Figure S20). These high oxidation potentials may be due to a limited stabilization of the distorted octahedral  $\text{Pd}^{\text{III}}$  center by the tridentate monoprotonated ligand, as well as the presence of a positive charge on the  $t^{\text{Bu}}\text{N}_4$  ligand.

**Electrochemical Oxidation Behavior of  $(t^{\text{Bu}}\text{N}_4)\text{Pd}^{\text{II}}\text{Cl}_2$ .** The synthesis of  $(t^{\text{Bu}}\text{N}_4)\text{Pd}^{\text{II}}\text{Cl}_2$  (**2**) has been previously reported,<sup>45,52</sup> and their conformational equilibria in solution have been studied by variable-temperature NMR.<sup>52</sup> In particular,  $(t^{\text{Bu}}\text{N}_4)\text{Pd}^{\text{II}}\text{Cl}_2$  was shown to exist in  $\text{CH}_2\text{Cl}_2$  as a mixture of two interconverting conformers  $(\kappa^2\text{-}t^{\text{Bu}}\text{N}_4)\text{Pd}^{\text{II}}\text{Cl}_2$  and  $(\kappa^3\text{-}t^{\text{Bu}}\text{N}_4)\text{Pd}^{\text{II}}\text{Cl}_2$  in a 2:3 ratio and with an activation energy for the  $\kappa^3$  to  $\kappa^2$  isomer interconversion of  $\Delta G^\ddagger = 14.9 \pm 0.2$  kcal/mol.<sup>52</sup>

In the report by Kress et al., the  $(\kappa^2\text{-}t^{\text{Bu}}\text{N}_4)\text{Pd}^{\text{II}}\text{Cl}_2$  conformation was characterized in the solid state by X-ray diffraction.<sup>52</sup> However, we were able to crystallize the other conformation,  $(\kappa^3\text{-}t^{\text{Bu}}\text{N}_4)\text{Pd}^{\text{II}}\text{Cl}_2$ , as dark red crystals obtained by diethyl diffusion of ether into a solution of **2** in  $\text{CH}_2\text{Cl}_2\text{-CHCl}_3$  (1:2 v/v). The X-ray structure of  $(\kappa^3\text{-}t^{\text{Bu}}\text{N}_4)\text{Pd}^{\text{II}}\text{Cl}_2$  reveals a Pd– $\text{N}_{\text{amine}}$  distance of 2.655 Å—slightly longer than the average Pd– $\text{N}_{\text{amine}}$  distances in the dicationic complex **1**—while the second amine points away from the metal (Figure 5a). The isolation and structural characterization of the

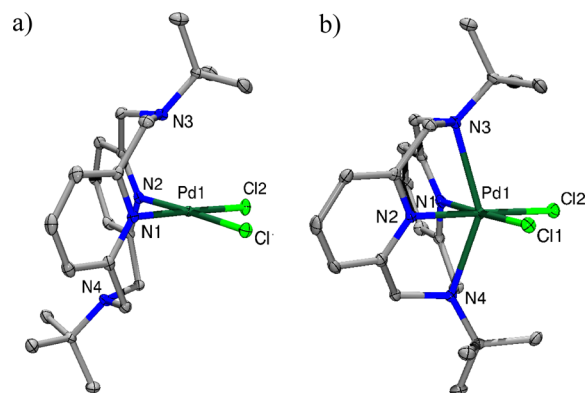


**Figure 5.** ORTEP representation (50% probability ellipsoids) of (a)  $[(\kappa^3\text{-}t^{\text{Bu}}\text{N}_4)\text{Pd}^{\text{II}}\text{Cl}_2]$ , **2**, and (b) the cation of  $[(t^{\text{Bu}}\text{N}_4)\text{Pd}^{\text{III}}\text{Cl}_2][\text{ClO}_4]_2^{2+}$ . Selected bond lengths (Å), (a): Pd1–N1 2.009(2); Pd1–N2 2.059(2); Pd1–N3 2.655(2); Pd1–Cl1 2.317(1); Pd1–Cl2 2.295(1). (b): Pd1–N12.007(2); Pd1–N2 1.999(2); Pd1–N3 2.398(2); Pd1–N4 2.436(2); Pd1–Cl1 2.312(1); Pd1–Cl2 2.320(1).

$(\kappa^3\text{-}t^{\text{Bu}}\text{N}_4)\text{Pd}^{\text{II}}\text{Cl}_2$  complex with  $t^{\text{Bu}}\text{N}_4$  acting as a tridentate ligand strongly supports the conformational flexibility of the ligand and its essential role in stabilizing high-valent Pd centers (see below).

The complex  $(t^{\text{Bu}}\text{N}_4)\text{Pd}^{\text{II}}\text{Cl}_2$  (**2**) reveals a more complex electrochemical behavior compared to that of  $[(t^{\text{Bu}}\text{N}_4)\text{Pd}^{\text{II}}(\text{MeCN})_2]^{2+}$ . The CV of **2** in 0.1 M  $\text{Bu}_4\text{NClO}_4/\text{CH}_2\text{Cl}_2$  exhibits three oxidation waves labeled as A, B, and C (Figure 6). When the scan direction is reversed after the first two oxidation waves (A and B), only one corresponding cathodic wave A' is observed during the reverse scan at slow scan rates, which was assigned as the reduction of  $[(\kappa^4\text{-}t^{\text{Bu}}\text{N}_4)\text{Pd}^{\text{III}}\text{Cl}_2]^+$  to  $(t^{\text{Bu}}\text{N}_4)\text{Pd}^{\text{II}}\text{Cl}_2$  (Figure 6a, blue line). This assignment was also confirmed by the CV of the isolated complex  $[(\kappa^4\text{-}t^{\text{Bu}}\text{N}_4)\text{-}$

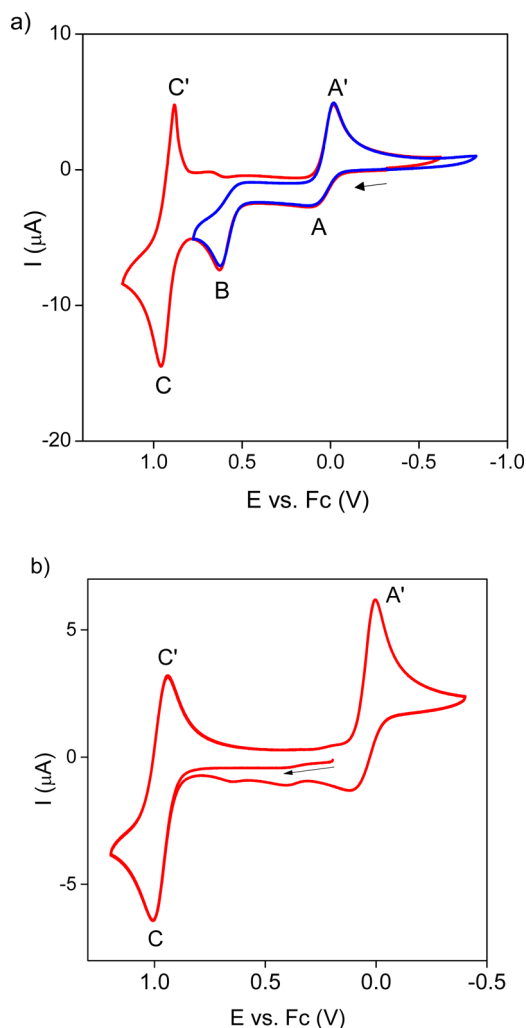


**Figure 6.** (a) CV of 2.5 mM  $(\text{tBu}_4\text{N})\text{Pd}^{\text{II}}\text{Cl}_2$  (**2**) in 0.1 M  $\text{Bu}_4\text{NClO}_4/\text{CH}_2\text{Cl}_2$  at (100 mV/s, RT):  $\text{Pd}^{\text{II/III}}$  range only (blue), and full range (red); (b) CV of 1.1 mM  $[(\text{tBu}_4\text{N})\text{Pd}^{\text{II}}\text{Cl}_2](\text{ClO}_4)$  in 0.1 M  $\text{Bu}_4\text{NPF}_6/\text{MeCN}$  (100 mV/s, RT).

$\text{Pd}^{\text{III}}\text{Cl}_2](\text{ClO}_4)_2$ ,  $2^+[\text{ClO}_4]$ , which was obtained as described below (Figure 6b). The first two oxidation waves A and B were thus assigned as the  $\text{Pd}^{\text{II}}/\text{Pd}^{\text{III}}$  oxidation of the two conformers of **2**, namely,  $(\kappa^4\text{-tBu}_4\text{N})\text{Pd}^{\text{II}}\text{Cl}_2$  and  $(\kappa^3\text{-tBu}_4\text{N})\text{Pd}^{\text{II}}\text{Cl}_2$ , respectively (vide infra). The quasireversible oxidation wave C observed at higher potential was assigned to the  $\text{Pd}^{\text{III}}/\text{Pd}^{\text{IV}}$  couple for the  $[(\kappa^4\text{-tBu}_4\text{N})\text{Pd}^{\text{III}}\text{Cl}_2]^+$  species. Although the shape of the reverse  $\text{Pd}^{\text{IV}}/\text{Pd}^{\text{III}}$  reduction peak suggests a small product adsorption effect,<sup>74</sup> the small separation between the forward (C) and reverse (C') peaks for the  $\text{Pd}^{\text{III}}/\text{Pd}^{\text{IV}}$  couple is consistent with a minimal conformational change upon oxidation of the distorted octahedral  $\text{Pd}^{\text{III}}$  species to an octahedral  $\text{Pd}^{\text{IV}}$  product. Although the  $(\text{tBu}_4\text{N})\text{Pd}^{\text{IV}}$  product was not isolated and structurally characterized due to its limited stability, the reported  $\text{Pd}^{\text{IV}}$  complexes stabilized by analogous  $\text{Me}_6\text{N}_4$  and  $\text{iPr}_4\text{N}_4$  ligands were shown to have a pseudo-octahedral geometry with a  $\kappa^4$ -coordinated ligand.<sup>47</sup>

To investigate the role of various ligand conformations during  $\text{Pd}^{\text{II/III}}$  oxidation, a variable scan rate CV study was performed (Figure 7). Interestingly, upon increasing the scan rate the ratio of peak currents  $i_{\text{pa}}$  for the oxidation waves A and B decreases significantly. For example, the peak current ratio

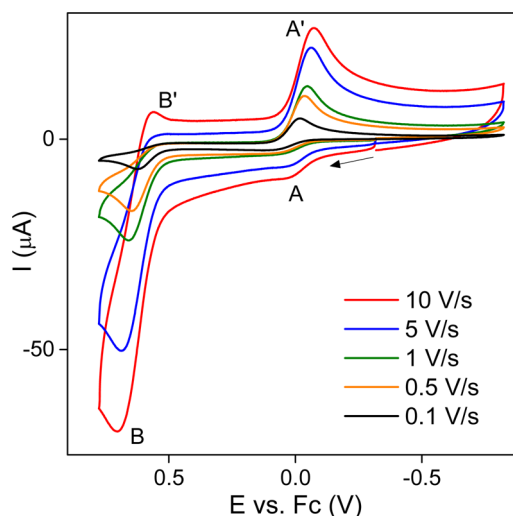


**Figure 7.** CV of 2.5 mM  $(\text{tBu}_4\text{N})\text{Pd}^{\text{II}}\text{Cl}_2$  (**2**) in 0.1 M  $\text{Bu}_4\text{NClO}_4/\text{CH}_2\text{Cl}_2$  at various scan rates at RT. Only the voltage range corresponding to  $\text{Pd}^{\text{II/III}}$  redox processes is shown.

$i_{\text{pa}}(\text{A})/i_{\text{pa}}(\text{B})$  changes from 1:1.5 to  $\sim 1:10$  upon increasing scan rate from 50 mV/s to 5 V/s, respectively. Moreover, the oxidation peak A has a characteristic sigmoidal shape indicative of a CE process (chemical reaction preceding electron transfer).<sup>74</sup> This observation, in addition to a small peak-to-peak separation between the anodic wave A and the reverse cathodic wave A'—assigned to the reduction of  $[(\kappa^4\text{-tBu}_4\text{N})\text{Pd}^{\text{III}}\text{Cl}_2]^+$  ( $\kappa^4\text{-2}^+$ ) ( $\Delta E_p \approx 130$  mV at 50 mV/s)—indicates that the low potential oxidation wave A can be assigned to the  $\text{Pd}^{\text{II}}/\text{Pd}^{\text{III}}$  oxidation for the minor isomer  $(\kappa^4\text{-tBu}_4\text{N})\text{PdCl}_2$  ( $\kappa^4\text{-2}$ ) that is not observed by NMR in solution, yet it can be generated through the  $(\kappa^3\text{-tBu}_4\text{N})\text{PdCl}_2$  ( $\kappa^3\text{-2}$ ) to  $(\kappa^4\text{-tBu}_4\text{N})\text{PdCl}_2$  ( $\kappa^4\text{-2}$ ) equilibrium during the slow anodic scan. As the  $\kappa^4\text{-2}$  conformer is being oxidized at a lower oxidation potential, the above isomer interconversion can thus funnel a large fraction of **2** to be oxidized through the  $\kappa^4\text{-2}$  isomer. The lower oxidation potential of ( $\kappa^4\text{-2}$ ) can be attributed to the axial coordination of the amine N atom to the Pd center that leads to an increase in the energy of the  $d_{z^2}$ -based highest occupied molecular orbital (HOMO). An analogous effect of axial donor coordination was previously suggested for Pd and Pt complexes with *fac*-chelating tridentate and other polydentate ligands that were found to exhibit uncommonly low oxidation potentials and to be much more reactive toward mild oxidants compared to the analogous complexes with simple bidentate N-donor ligands.<sup>24,29,31,32,41,79</sup>

The experimental variable scan rate CVs showing the  $\text{Pd}^{\text{II}}/\text{Pd}^{\text{III}}$  oxidation events were simulated using the ESP electrochemical simulation package,<sup>56,57</sup> and the parameters were optimized against experimental data using the best-fitting routine for nonlinear optimization implemented in ESP. A good agreement between simulated and experimental data was achieved using the proposed mechanism shown in Scheme 4 (Figure 8). This mechanism implies that the conformational change to form  $\kappa^4\text{-2}$  occurs prior to oxidation (CE mechanism), and the apparent irreversibility of the  $\kappa^3\text{-2}$  oxidation at slow scan rates is due to the fast interconversion of  $\kappa^3\text{-2}^+$  to form the isolated species  $\kappa^4\text{-2}^+$  (i.e., an EC mechanism: electron transfer followed by chemical reaction).<sup>74</sup> Indeed, the oxidation wave B assigned to  $\kappa^3\text{-2}$  oxidation shows a corresponding reverse cathodic peak appearing at fast scan rates ( $\geq 10$  V/s), as the  $\kappa^3\text{-2}$

**Scheme 4. Mechanism Used for Simulation of Variable Scan Rate CVs of  $(\text{t}^{\text{Bu}}\text{N4})\text{Pd}^{\text{II}}\text{Cl}_2$  (2.5 mM in 0.1 M  $\text{Bu}_4\text{NClO}_4/\text{CH}_2\text{Cl}_2$ , 298 K)<sup>a</sup>**

Electron transfer steps:	E (mV vs. Fc):	$k_e$ (cm/s):
$\kappa^3\text{-2}^+ + e^- \xrightleftharpoons[B]{B'} \kappa^3\text{-2}$	622.5	0.1
$\kappa^4\text{-2}^+ + e^- \xrightleftharpoons[A]{A'} \kappa^4\text{-2}$	-68.5	0.1
Chemical reactions:	$k_f$ (1/s):	$k_b$ (1/s):
$\kappa^2\text{-2} \xrightleftharpoons[k_b]{k_f} \kappa^3\text{-2}$	77.76	39.02
$\kappa^3\text{-2} \xrightleftharpoons[k_b]{k_f} \kappa^4\text{-2}$	35.98	6083
$\kappa^3\text{-2}^+ \xrightarrow{k_f} \kappa^4\text{-2}^+$	121.5	0

<sup>a</sup>The experimental and simulated CVs are shown in Figure 8. Notation: **2** is  $(\text{t}^{\text{Bu}}\text{N4})\text{Pd}^{\text{II}}\text{Cl}_2$ ,  $2^+$  is  $[(\text{t}^{\text{Bu}}\text{N4})\text{Pd}^{\text{III}}\text{Cl}_2]^+$ .

$2^+$  to  $\kappa^4\text{-2}^+$  interconversion is not complete on the CV time scale at fast scan rates (Figure 8). It is important to note that, while the best-fit parameters used for the CV simulations and shown in Scheme 4 produce good fits to the experimental data (Figure 8), the ESP simulation package does not provide errors for the obtained parameters, given the complex mechanism and the multiple species involved in these reactions. Therefore, it is

better to consider these parameters as being semiquantitative at best.

The one-electron oxidation product of **2** was obtained by controlled potential electrolysis in  $\text{Bu}_4\text{NClO}_4/\text{CH}_2\text{Cl}_2$  and isolated in 78% yield. The X-ray structure of  $[(\kappa^4\text{-t}^{\text{Bu}}\text{N4})\text{Pd}^{\text{III}}\text{Cl}_2]\text{ClO}_4$  ( $2^+[\text{ClO}_4]$ ) reveals a distorted octahedral geometry around the  $\text{Pd}^{\text{III}}$  center, with  $\text{Pd}-\text{N}_{\text{amine}}$  distances of 2.398 and 2.436 Å, similar to the other  $(\text{t}^{\text{Bu}}\text{N4})\text{Pd}^{\text{III}}$  complexes,<sup>44,45</sup> yet  $\sim 0.24$  Å shorter than the  $\text{Pd}-\text{N}_{\text{amine}}$  distance in  $(\kappa^3\text{-t}^{\text{Bu}}\text{N4})\text{Pd}^{\text{II}}\text{Cl}_2$  and as expected for the stronger interactions with the oxidized  $\text{Pd}^{\text{III}}$  center. The EPR spectrum of the isolated  $[(\text{t}^{\text{Bu}}\text{N4})\text{Pd}^{\text{III}}\text{Cl}_2]\text{ClO}_4$  in  $\text{PrCN}-\text{MeCN}$  (3:1 v/v) at 77 K reveals a nearly axial signal with superhyperfine coupling to the two axial N atoms:  $g_x = 2.152$  ( $A_N = 14.0$  G),  $g_y = 2.142$  ( $A_N = 18.0$  G),  $g_z = 2.000$  ( $A_N = 23.0$  G, Figure 9). The CV of  $2^+[\text{ClO}_4]$  in  $\text{Bu}_4\text{NPF}_6/\text{MeCN}$  exhibits a reduction wave assigned to the  $\text{Pd}^{\text{III/II}}$  couple at a potential similar to that observed for the oxidation of the  $(\kappa^4\text{-t}^{\text{Bu}}\text{N4})\text{Pd}^{\text{II}}\text{Cl}_2$  isomer (wave A' in Figure 6a), thus supporting the essential role of the  $\kappa^4$  conformation in the facile oxidation of **2**. In addition,  $2^+[\text{ClO}_4]$  exhibits the expected reversible  $\text{Pd}^{\text{III/IV}}$  oxidation wave at  $E_{1/2} = 975$  mV versus Fc ( $\Delta E_p = 68$  mV, Figure 6b).

Overall, although the two major conformers of  $(\text{t}^{\text{Bu}}\text{N4})\text{Pd}^{\text{II}}\text{Cl}_2$  present in solution are  $\kappa^2\text{-2}$  and  $\kappa^3\text{-2}$ , the detailed CV studies described above suggest that the oxidation behavior of **2** is mainly determined by the two most easily oxidized conformers, namely,  $\kappa^4\text{-2}$  and  $\kappa^3\text{-2}$ . However, the redox waves corresponding to the  $(\kappa^2\text{-t}^{\text{Bu}}\text{N4})\text{Pd}$  isomers can be observed at fast scan rates or at low temperatures, as these conditions hamper the proposed interconversion equilibria (see below).

**Electrochemical Oxidation Behavior of  $[(\text{t}^{\text{Bu}}\text{N4})\text{Pd}^{\text{II}}\text{Me}(\text{MeCN})](\text{OTf})$  (**3**)<sup>+</sup>.** The complex  $[(\text{t}^{\text{Bu}}\text{N4})\text{Pd}^{\text{II}}\text{Me}(\text{MeCN})](\text{OTf})$

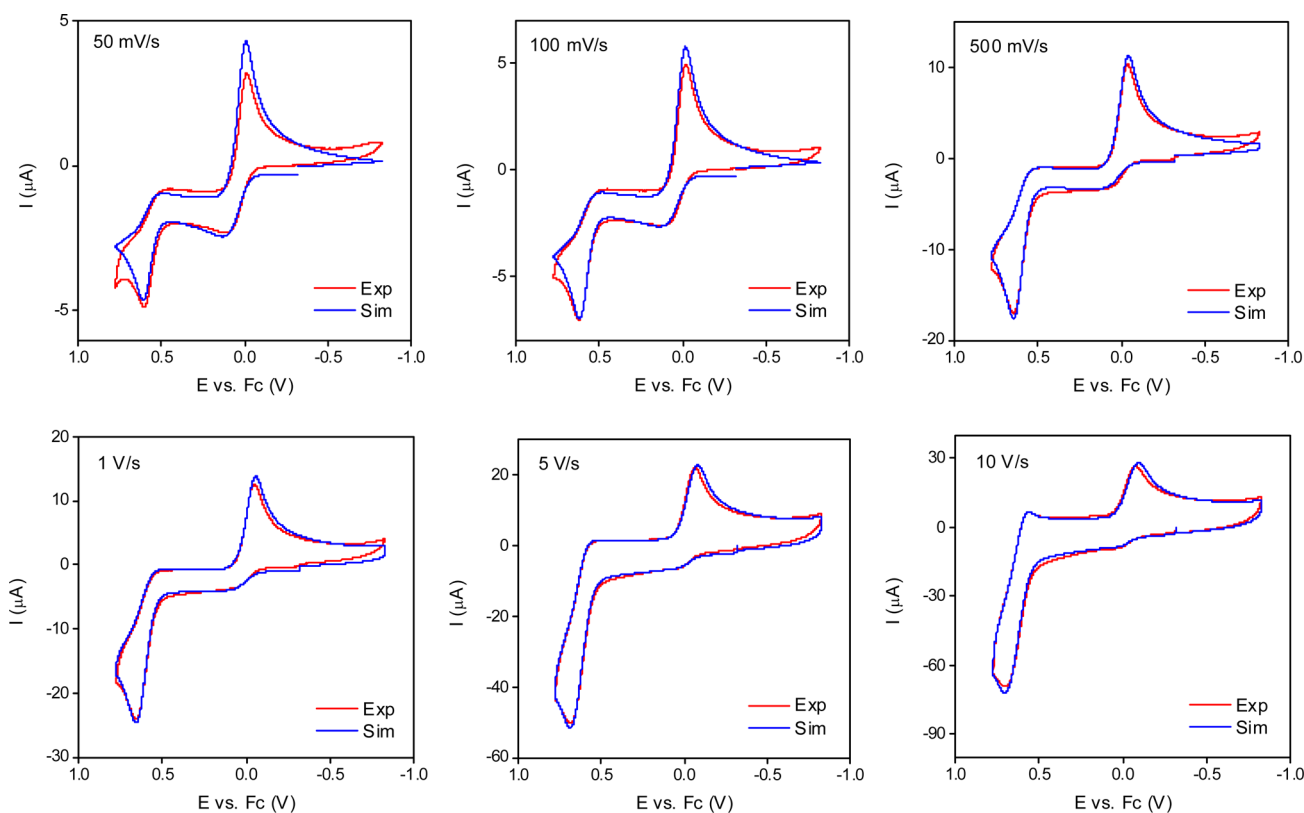


**Figure 8.** Experimental (red) and simulated (blue) CVs of 2.5 mM  $(\text{t}^{\text{Bu}}\text{N4})\text{Pd}^{\text{II}}\text{Cl}_2$  (**2**) in 0.1 M  $\text{Bu}_4\text{NClO}_4/\text{CH}_2\text{Cl}_2$  at various scan rates at RT.

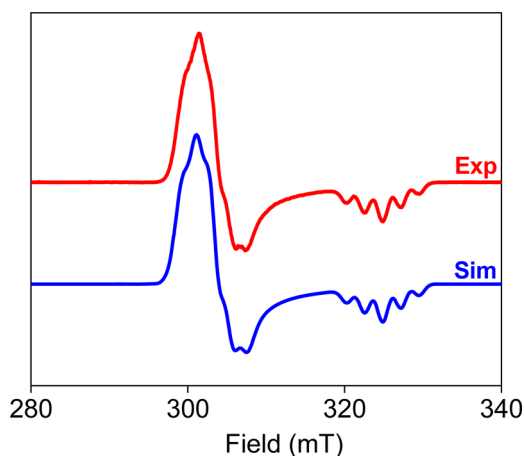


**Figure 9.** (red line) EPR spectrum of  $[(\text{tBu}_4\text{N})\text{Pd}^{\text{III}}\text{Cl}_2](\text{ClO}_4)$  in PrCN/MeCN (3:1 v/v) at 77 K. (blue line) Simulated spectrum. Parameters used for simulation:  $g_x = 2.152$  ( $A_N = 14.0$  G),  $g_y = 2.142$  ( $A_N = 18.0$  G),  $g_z = 2.000$  ( $A_N = 23.0$  G).

( $3^+[\text{OTf}]$ ) was synthesized according to the previously published procedure.<sup>52</sup> According to the NMR studies by Kress et al.,  $3^+$  exhibits a conformational equilibrium in solution similar to  $(\text{tBu}_4\text{N})\text{Pd}^{\text{II}}\text{Cl}_2$ , with two major conformers ( $\kappa^2\text{-tBu}_4\text{N}$ )Pd and ( $\kappa^3\text{-tBu}_4\text{N}$ )Pd being present in solution in a 3:4 ratio, and a  $\kappa^3\text{-}3^+$  to  $\kappa^2\text{-}3^+$  isomer interconversion activation energy of  $14.5 \pm 0.2$  kcal/mol.<sup>52</sup> Therefore, the electrochemical behavior of  $3^+$  is expected to be similar to that of **2**. Indeed, the CVs of  $[(\text{tBu}_4\text{N})\text{Pd}^{\text{II}}\text{Me}(\text{MeCN})]^+$  in 0.1 M  $\text{Bu}_4\text{NClO}_4/\text{MeCN}$  at scan rates ranging from 20 mV/s to 1 V/s exhibit two oxidation waves A and B assigned as the  $\text{Pd}^{\text{II}/\text{III}}$  oxidations for the two conformers  $\kappa^4\text{-}3^+$  and  $\kappa^3\text{-}3^+$ , respectively (Figure 10),

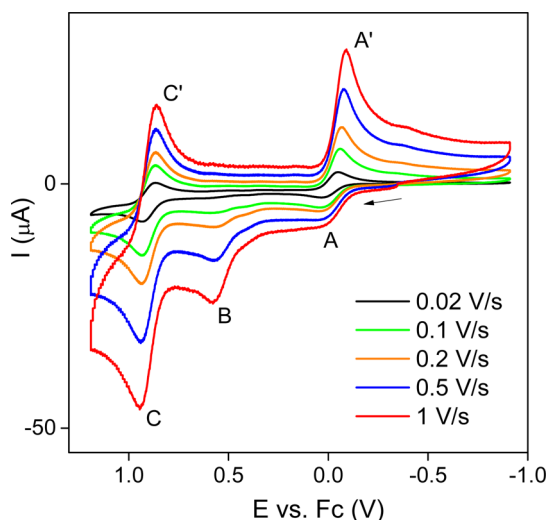


**Figure 10.** CV of 2.8 mM  $[(\text{tBu}_4\text{N})\text{Pd}^{\text{II}}\text{Me}(\text{MeCN})](\text{OTf})$  ( $3^+[\text{OTf}]$ ) in 0.1 M  $\text{Bu}_4\text{NClO}_4/\text{MeCN}$  at various scan rates at RT.

while the reversible redox wave at higher potential was assigned to the  $(\kappa^4\text{-tBu}_4\text{N})\text{Pd}^{\text{III}}/(\kappa^4\text{-tBu}_4\text{N})\text{Pd}^{\text{IV}}$  oxidation couple (the C/C' waves in Figure 10). Similar to **2**, the ratio of peak currents of waves A and B,  $i_{\text{pa}}(\text{A})/i_{\text{pa}}(\text{B})$  decreases with increasing scan rates from 1:0.4 at 100 mV/s to 1:1.7 at 1 V/s, and the sigmoidal shape of the anodic wave A becomes apparent at scan rates  $>0.5$  V/s (Figure 10).<sup>74</sup>

To get further insight into the conformation equilibria involved during the electrochemical oxidation of complex  $3^+$ , variable-temperature CV and differential pulse voltammetry (DPV) studies were performed in a temperature range from  $-70$  °C to  $+20$  °C in  $\text{Bu}_4\text{NBF}_4/\text{EtCN}$ . Propionitrile was used as a solvent because of its lower freezing point compared to MeCN. The complex  $[(\text{tBu}_4\text{N})\text{Pd}^{\text{II}}\text{Me}(\text{EtCN})](\text{OTf})$ ,  $3\text{a}^+[\text{OTf}]$ , was obtained by dissolving **3** in EtCN or by a procedure analogous to that described for the synthesis of **3** except for using EtCN as the solvent. The electrochemical behavior of  $3\text{a}^+[\text{OTf}]$  is very similar to that of  $3^+[\text{OTf}]$  (Figures 9–11), indicative of analogous conformational equilibria in solution.

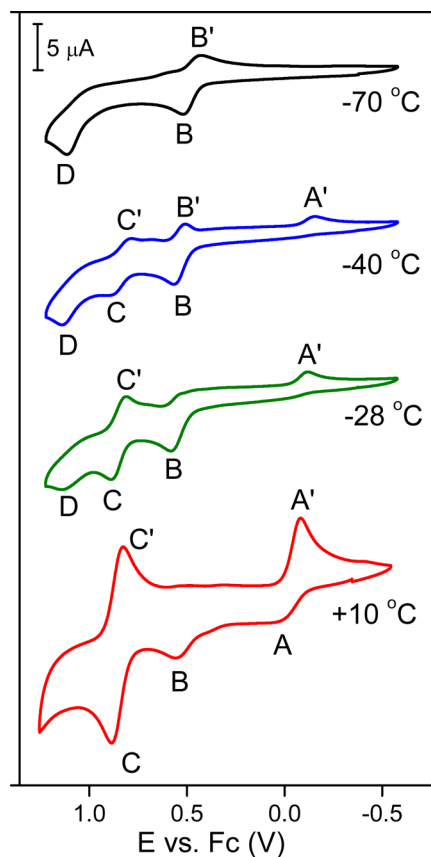


**Figure 11.** Variable-temperature CVs of  $[(\text{tBu}_4\text{N})\text{Pd}^{\text{II}}\text{Me}(\text{EtCN})]^+$  ( $3\text{a}^+$ ) in 0.1 M  $\text{Bu}_4\text{NBF}_4/\text{EtCN}$  (100 mV/s).

Interestingly, lowering the temperature to  $-70$  °C leads to an entirely different CV in EtCN compared to that observed at RT (Figure 11). Only two oxidation waves were observed at  $-70$  °C: a quasireversible oxidation wave B assigned as  $\kappa^3\text{-}3\text{a}^+ \text{Pd}^{\text{II}/\text{III}}$  oxidation and an electrochemically irreversible wave D assigned as  $\kappa^2\text{-}3\text{a}^+ \text{Pd}^{\text{II}/\text{III}}$  oxidation (Figure 11). Therefore, the CV at  $-70$  °C likely represents a case where the conformational equilibrium of  $[(\text{tBu}_4\text{N})\text{Pd}^{\text{II}}\text{Me}(\text{EtCN})]^+$  in solution is essentially “frozen”, and only the two major conformers,  $\kappa^3\text{-}3\text{a}^+$  and  $\kappa^2\text{-}3\text{a}^+$ , give rise to the observed oxidation waves. Remarkably, the quasi-reversibility of the  $\kappa^3\text{-}3\text{a}^+ \text{Pd}^{\text{II}/\text{III}}$  oxidation indicates that even a tridentate coordination of  $\text{tBu}_4\text{N}$  may be sufficient for stabilizing the  $\text{Pd}^{\text{III}}$  oxidation state, which could be achieved either through the formation of a five-coordinate species or a six-coordinate species with an EtCN molecule bound in the axial position. By comparison, increasing

the temperature leads to a decrease of the reverse cathodic peak B' of the  $\kappa^3\text{-3a}^+$  Pd<sup>II/III</sup> redox couple and to the appearance of the reversible  $\kappa^4\text{-3a}^{2+}$  Pd<sup>III/IV</sup> redox wave (C/C' in Figure 11) as well as the  $\kappa^4\text{-3a}^{2+}$  Pd<sup>III/II</sup> reverse cathodic wave (A' in Figure 11), indicative of an increased contribution of the ( $\kappa^4\text{-N4}$ )Pd conformations at higher temperatures. Overall, the apparent electrochemical irreversibility of the  $\kappa^3\text{-3a}^+$  Pd<sup>II/III</sup> oxidation at RT is likely due to the fast conversion of the Pd<sup>III</sup> product  $\kappa^3\text{-3a}^{2+}$  to a more stable  $\kappa^4\text{-3a}^{2+}$  conformation (i.e., an EC mechanism).<sup>74</sup> Similarly, the differential pulse voltammograms (DPVs) of complex  $3\text{a}^+$  recorded at various temperatures show clearly the disappearance of the oxidation peak D and the growth of the oxidation peaks A and C as the temperature is increased (Figure 12). Since the low temperatures are expected

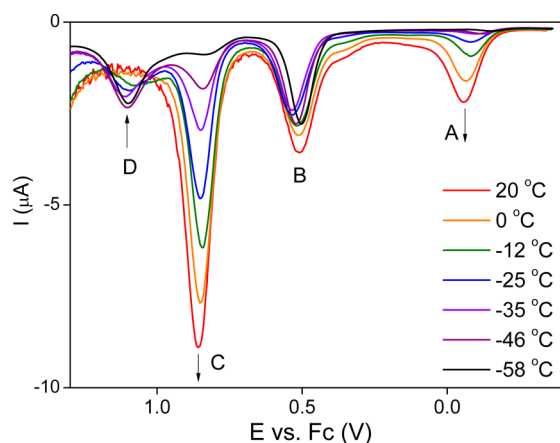


**Figure 12.** Variable-temperature DPVs of  $[(\text{tBu}_4\text{N})\text{Pd}^{\text{II}}\text{Me}(\text{EtCN})]^+$  ( $3\text{a}^+$ ) in 0.1 M  $\text{Bu}_4\text{NBF}_4/\text{EtCN}$  (pulse amplitude 0.05 V). Arrows indicate the change of peak height upon warming the solution from  $-58$  to  $20$  °C.

to limit the equilibration between the different conformations, these DPVs further support the proposed conformational changes based on the variable scan rate CV studies.

The redox behavior of  $3\text{a}^+$  was also investigated using variable scan rate CVs. The Pd<sup>II/III</sup> oxidation wave corresponding to the  $\kappa^2\text{-3a}^+$  isomer (wave D in Figures 11 and 12) appears only at scan rates higher than 5 V/s (Figure 13 and Supporting Information, Figure S30). Using a mechanism similar to the one proposed for complex **1**, we were able to simulate the experimental CVs at variable scan rates using the ESP program. The mechanism used for the simulation and the optimized parameters are given in Scheme 5. A good fit between experimental data and simulated CV scans supports the viability of the proposed mechanism (Figure 13) and allows a semi-quantitative comparison between the redox potentials of various conformers and the corresponding rates of interconversion. Importantly, the rate constants and equilibrium constant for the  $\kappa^2\text{-3a}^+$  and  $\kappa^3\text{-3a}^+$  interconversion ( $k_f = 114 \text{ s}^{-1}$ ,  $k_b = 152 \text{ s}^{-1}$ ,  $K_{\text{eq}} = k_f/k_b = 1.33$ ) obtained from the best-fit optimization of the CV simulations are in good agreement with the NMR experimental data reported previously ( $\Delta G^\ddagger$  of 14.5 kcal/mol for  $\kappa^3\text{-3a}^+$  and a 3:4 ratio of  $\kappa^2\text{-3a}^+/\kappa^3\text{-3a}^+$ ).<sup>52</sup> In addition, the electrochemical studies and digital CV simulations presented herein provide strong evidence for the key role of the minor isomer  $\kappa^4\text{-3a}^+$  in the observed redox reactivity, information that cannot be obtained from NMR studies. Although the minor isomer  $\kappa^4\text{-3a}^+$  is not observed by NMR and

is present in solution only in a small fraction (<1%), it is most likely responsible for the unique facile oxidation of these Pd<sup>II</sup> complexes.

Remarkably, the coordination of an axial amine donor leads to a dramatic lowering of the Pd<sup>II/III</sup> oxidation potential, as observed by CV and DPV studies (Figures 11–13) and digital CV simulations (Scheme 5). For instance, the potentials for Pd<sup>II/III</sup> couples obtained by CV for conformers  $\kappa^4\text{-3a}^+$  ( $-142.5 \text{ mV vs Fc}$ ) and  $\kappa^3\text{-3a}^+$  ( $437.5 \text{ mV vs Fc}$ ) differ by 580 mV, while the potential for the latter is 601 mV more negative compared to that for the  $\kappa^2\text{-3a}^+$  conformer (1038.5 mV). Similar values are obtained from DPV scans, with the peak potential differences of 564 mV and 592 mV between A ( $\kappa^4\text{-3a}^+$ ) and B ( $\kappa^3\text{-3a}^+$ ) and between B and D ( $\kappa^2\text{-3a}^+$ ), respectively (Figure 12). Overall, these electrochemical studies provide an estimate for the effect of axial N-donor ligands on the oxidation potential of the corresponding Pd<sup>II</sup> complexes, each axial ligand lowering the Pd<sup>II/III</sup> potentials by  $\sim 600 \text{ mV}$ . Importantly, this estimate can be informative when designing ligands for oxidation reactivity studies, especially since it is becoming evident that multidentate ligands with axial donors can promote reactions with mild oxidants.<sup>22–27</sup>

Formation of the Pd<sup>III</sup> product was further investigated by low-temperature electrolysis of  $[(\text{tBu}_4\text{N})\text{Pd}^{\text{II}}\text{Me}(\text{EtCN})]^+$  ( $3\text{a}^+$ ) and monitored by UV–vis. When  $3\text{a}^+$  was electrooxidized at 0.78 V versus Fc in  $\text{Bu}_4\text{NClO}_4/\text{EtCN}$  at  $-65$  °C, the formation of a dark blue product was observed that is characterized by intense absorption bands at 614 nm ( $\epsilon = 1700 \text{ M}^{-1} \text{ cm}^{-1}$ ) and 371 nm ( $\epsilon = 3000 \text{ M}^{-1} \text{ cm}^{-1}$ , Figure 14), assigned to the  $[(\text{tBu}_4\text{N})\text{Pd}^{\text{III}}\text{Me}(\text{EtCN})]^{2+}$  ( $3\text{a}^{2+}$ ) complex. Its EPR spectrum in EtCN at 77 K reveals a rhombic EPR signal with g values of 2.199, 2.115, and 2.009, and superhyperfine coupling to the two axial N atoms in the z direction ( $A_N = 20 \text{ G}$ ), consistent with the presence of a Pd<sup>III</sup> center in a  $d_z^2$  ground state (Figure 15).

While the  $[(\text{tBu}_4\text{N})\text{Pd}^{\text{III}}\text{Me}(\text{EtCN})]^{2+}$  complex obtained by electrolysis could not be crystallized, the analogous acetonitrile complex can be obtained by chloride abstraction with  $\text{AgOTf}$  from  $[(\text{tBu}_4\text{N})\text{Pd}^{\text{III}}\text{MeCl}](\text{BF}_4)$ <sup>44</sup> in MeCN at RT (Scheme 6). Although the conversion was not complete even after seven weeks, the product could be crystallized by diffusion of ether at  $-20$  °C as a triflate salt  $[(\text{tBu}_4\text{N})\text{Pd}^{\text{III}}\text{Me}(\text{MeCN})](\text{OTf})_2 \cdot 3^{2+}[\text{OTf}]_2$ , and characterized by X-ray, UV–vis, EPR, ESI-MS. The X-ray analysis of  $3^{2+}[\text{OTf}]_2$  reveals a distorted octahedral Pd center with elongated axial Pd–N<sub>amine</sub> bond distances (2.399 and 2.397 Å) compared to the equatorial Pd–N<sub>py</sub> bond lengths (2.004 and 2.076 Å, Figure 16), and similar to other previously described  $(\text{tBu}_4\text{N})\text{Pd}^{\text{III}}$  complexes.<sup>44,45</sup> At the same time, the Pd–N<sub>amine</sub> distances are 0.27–0.28 Å shorter compared to the monocationic complex  $[(\text{tBu}_4\text{N})\text{Pd}^{\text{III}}\text{MeCl}](\text{BF}_4)$ <sup>44</sup> likely due to the stronger interactions with the dicationic Pd<sup>III</sup> center in  $[(\text{tBu}_4\text{N})\text{Pd}^{\text{III}}\text{Me}(\text{MeCN})]^{2+}$ .

Overall, the low-temperature electrochemical behavior of  $3\text{a}^+$  is governed by the most stable conformations present in solution, namely,  $\kappa^2\text{-3a}^+$  and  $\kappa^3\text{-3a}^+$ , as the conformer interconversions at  $-60$  °C are slower than the time scale of the CV and DPV experiments. By contrast, at RT the main contributors to the electrochemical behavior are the two most easily oxidized conformers,  $\kappa^3\text{-3a}^+$  and the minor isomer  $\kappa^4\text{-3a}^+$ . This allows for the distinct observation of all three conformers at different temperatures and determination of their individual oxidation potentials. Remarkably, the conformations of the  $\text{tBu}_4\text{N}$  ligand have a profound effect on the oxidation potential of the corresponding Pd<sup>II</sup> complexes: the coordination of each axial amine

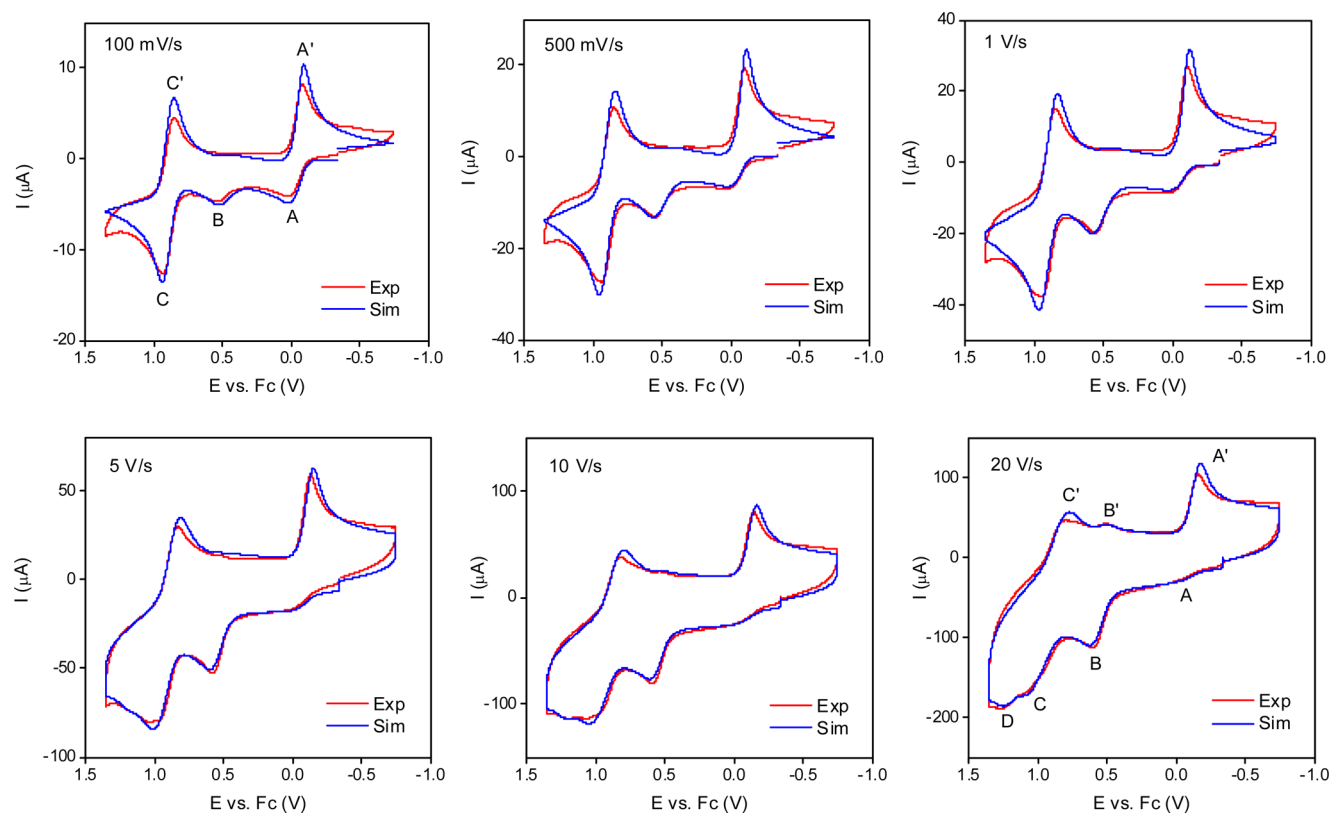


Figure 13. Experimental (red) and simulated (blue) CVs of 2.0 mM  $[(\text{tBu}_4\text{N})\text{PdMe}(\text{EtCN})]^+$  ( $3\text{a}^+$ ) in 0.1 M  $\text{Bu}_4\text{NPF}_6/\text{EtCN}$  at various scan rates at RT.

**Scheme 5. Mechanism Used for Simulation of Variable Scan Rate CVs of  $[(\text{tBu}_4\text{N})\text{PdMe}(\text{EtCN})]^+$  (2.0 mM in 0.1 M  $\text{Bu}_4\text{NPF}_6/\text{EtCN}$ , 298 K)<sup>a</sup>**

Electron transfer steps:	E (mV vs. Fc):	$k_e$ (cm/s):
$\kappa^2\text{-}3\text{a}^{2+} + \text{e}^- \xrightleftharpoons[\text{D}]{\text{D}'} \kappa^2\text{-}3\text{a}^+$	1038.5	0.005875
$\kappa^4\text{-}3\text{a}^{3+} + \text{e}^- \xrightleftharpoons[\text{C}]{\text{C}'} \kappa^4\text{-}3\text{a}^{2+}$	894.5	0.01187
$\kappa^3\text{-}3\text{a}^{2+} + \text{e}^- \xrightleftharpoons[\text{B}]{\text{B}'} \kappa^3\text{-}3\text{a}^+$	437.5	0.005281
$\kappa^4\text{-}3\text{a}^{2+} + \text{e}^- \xrightleftharpoons[\text{A}]{\text{A}'} \kappa^4\text{-}3\text{a}^+$	-142.5	0.518

Chemical reactions:	$k_f$ (1/s):	$k_b$ (1/s):
$\kappa^2\text{-}3\text{a}^+ \xrightleftharpoons[k_b]{k_f} \kappa^3\text{-}3\text{a}^+$	113.9	151.9
$\kappa^3\text{-}3\text{a}^+ \xrightleftharpoons[k_b]{k_f} \kappa^4\text{-}3\text{a}^+$	111.4	4457.5
$\kappa^3\text{-}3\text{a}^{2+} \xrightarrow{k_f} \kappa^4\text{-}3\text{a}^{2+}$	352.5	0
$\kappa^2\text{-}3\text{a}^{2+} \xrightarrow{k_f} \kappa^3\text{-}3\text{a}^{2+}$	352.5	0

<sup>a</sup>The experimental and simulated CVs are shown in Figure 13. Notation:  $3\text{a}^+$  is  $[(\text{tBu}_4\text{N})\text{Pd}^{\text{II}}\text{Me}(\text{EtCN})]^+$ ,  $3\text{a}^{2+}$  is  $[(\text{tBu}_4\text{N})\text{Pd}^{\text{III}}\text{Me}(\text{EtCN})]^{2+}$ , and  $3\text{a}^{3+}$  is  $[(\text{tBu}_4\text{N})\text{Pd}^{\text{IV}}\text{Me}(\text{EtCN})]^{3+}$ .

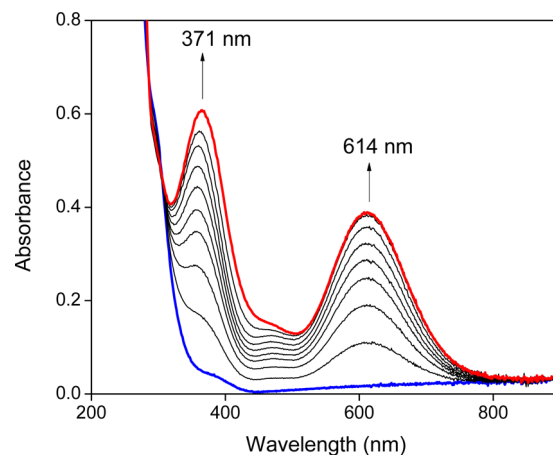
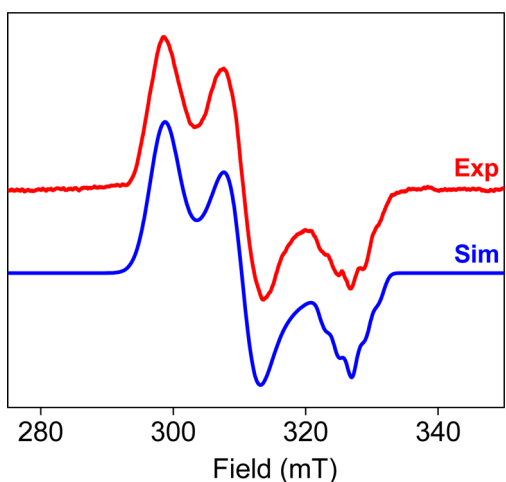


Figure 14. UV-vis spectra of the electrooxidation of  $[(\text{tBu}_4\text{N})\text{Pd}^{\text{II}}\text{Me}(\text{EtCN})](\text{OTf})$  in 0.1 M  $\text{Bu}_4\text{NClO}_4/\text{EtCN}$  (2.2 mM solution, 1 mm path length,  $-65^\circ\text{C}$ ,  $\Delta t = 12$  min). Arrows indicate the change of the band intensities over time.

**Electrochemical Oxidation Behavior of  $(\text{tBu}_4\text{N})\text{-Pd}^{\text{II}}\text{MeCl}$  (4).** To further investigate the effect of ligand flexibility on the metal complex redox properties, we explored the electrochemical behavior of a neutral monomethyl complex  $(\text{tBu}_4\text{N})\text{PdMeCl}$  (4), which exhibits a conformational behavior in solution that is different from the complexes described above. Complex 4 was synthesized as described previously<sup>52</sup> and was characterized by X-ray diffraction in this study (Figure 17). The X-ray structure of  $(\text{tBu}_4\text{N})\text{Pd}^{\text{II}}\text{MeCl}$  reveals a square planar geometry around the  $\text{Pd}^{\text{II}}$  center, with  $\text{tBu}_4\text{N}$  in the  $\kappa^2$  bidentate conformation and the two amine N atoms pointing

donor lowers the  $\text{Pd}^{\text{II/III}}$  oxidation potential by  $\sim 600$  mV and thus allows for the facile oxidation and isolation of the corresponding high-valent Pd complexes.



**Figure 15.** (red line) EPR spectrum of  $[(t\text{Bu}_4\text{N}_4)\text{Pd}^{\text{III}}\text{Me}(\text{EtCN})]^{2+}$  ( $3^{2+}$ ) in EtCN, 77 K. (blue line) Simulated spectrum. Parameters used for simulation:  $g_x = 2.199$ ;  $g_y = 2.115$ ;  $g_z = 2.009$  ( $A_N = 20$  G).

**Scheme 6. Synthesis of  $[(t\text{Bu}_4\text{N}_4)\text{Pd}^{\text{III}}\text{Me}(\text{RCN})]^{2+}$  ( $\text{R} = \text{Et}, \text{Me}$ )**

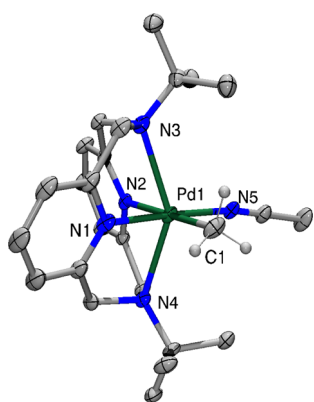
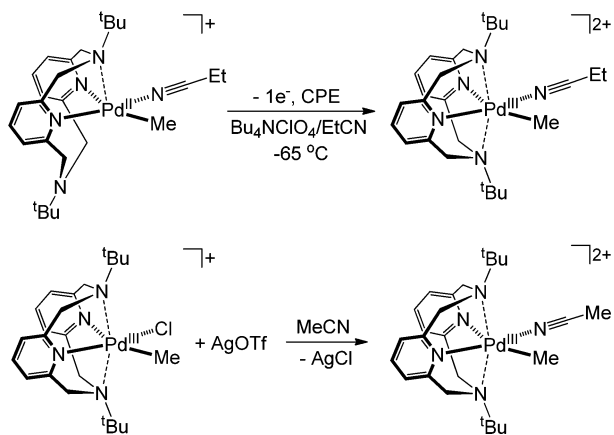


**Figure 16.** ORTEP representation (50% probability ellipsoids) of the cation of  $[(t\text{Bu}_4\text{N}_4)\text{Pd}^{\text{III}}\text{Me}(\text{MeCN})](\text{OTf})_2$  ( $3^{2+}[\text{OTf}]_2$ ). Selected bond lengths (Å): Pd1–N1 2.004(3); Pd1–N2 2.076(3); Pd1–N3 2.399(3); Pd1–N4 2.397(3); Pd1–N5 2.044(3); Pd1–C1 2.050(3).

away from the Pd center. This is consistent with the solution NMR studies of Kress et al. suggesting a single conformer present in solution and assigned as  $(\kappa^2\text{-}t\text{Bu}_4\text{N}_4)\text{Pd}^{\text{II}}\text{MeCl}$ .<sup>52</sup>

Given this geometry, one might expect that the oxidation potential of  $(\kappa^2\text{-}t\text{Bu}_4\text{N}_4)\text{Pd}^{\text{II}}\text{MeCl}$  is similar to the analogous

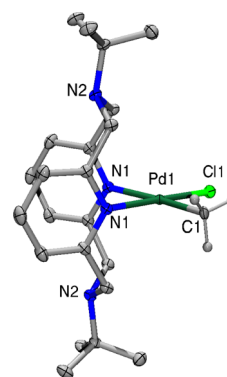


**Figure 17.** ORTEP representation (50% probability ellipsoids) of  $(t\text{Bu}_4\text{N}_4)\text{Pd}^{\text{II}}\text{MeCl}$  (**4**). Selected bond lengths (Å): Pd1–N1 2.116(1); Pd1–C1 2.055(3); Pd1–Cl1 2.291(1).

$(\text{L})\text{Pd}^{\text{II}}\text{MeCl}$  complexes, where L is a bidentate N-donor ligand. For instance, the CVs of  $(t\text{Bu}_2\text{bipy})\text{PdMeCl}$  ( $t\text{Bu}_2\text{bipy} = 4,4'$ -di-*tert*-butyl-2,2'-bipyridine) and  $(\text{tmeda})\text{PdMeCl}$  ( $\text{tmeda} = N,N,N',N'$ -tetramethylethylenediamine) reveal irreversible oxidation waves at relatively high potentials,  $\sim 0.7$ – $0.8$  V versus Fc, that do not become reversible even at high scan rates (Supporting Information, Figures S25 and S26). However, the CV of  $(t\text{Bu}_4\text{N}_4)\text{Pd}^{\text{II}}\text{MeCl}$  exhibits oxidation waves at much lower potentials and can be oxidized with mild oxidants such as ferrocenium to produce the stable complex  $[(\kappa^4\text{-}t\text{Bu}_4\text{N}_4)\text{Pd}^{\text{III}}\text{MeCl}]^+$  ( $4^+$ ).<sup>44</sup> To investigate whether such low potentials are indeed due to a conformational change and formation of the  $(\kappa^3\text{-}t\text{Bu}_4\text{N}_4)\text{PdMeCl}$  conformer—as opposed to just stabilization of the oxidized product—variable scan rate and temperature electrochemical studies were performed. The CV of **4** in 0.3 M  $\text{Bu}_4\text{NBF}_4/\text{CH}_2\text{Cl}_2$  exhibits several oxidation waves whose relative intensities depend on the scan rate and temperature. At slow scan rates ( $< 5$  V/s), only two oxidation waves were observed, labeled as B ( $E_{\text{pa}} \approx 0.14$  V vs Fc) and C ( $E_{1/2} = 0.60$  V vs Fc,  $\Delta E_{\text{p}} = 70$  mV) and assigned as  $\text{Pd}^{\text{II}/\text{III}}$  and  $\text{Pd}^{\text{III}/\text{IV}}$  oxidations, respectively (Figure 18). The anodic peak B is essentially electrochemically irreversible at RT, with the reverse cathodic peak B' appearing only at high scan rates  $\geq 7$  V/s. However, the anodic peak B is chemically reversible, and when the scan direction is reversed immediately past peak B, the corresponding cathodic wave A' assigned as a  $\text{Pd}^{\text{III}/\text{II}}$

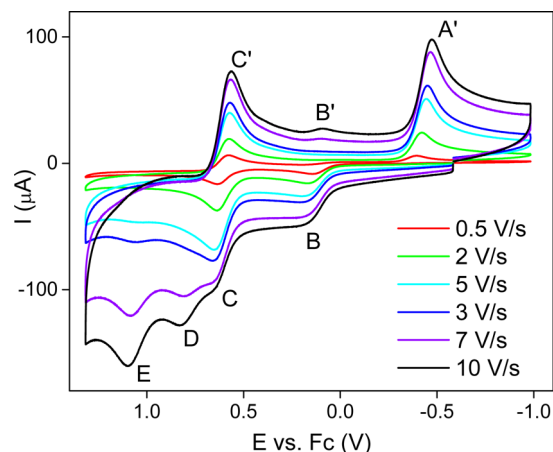


**Figure 18.** Variable scan rate CVs of 2.0 mM  $(t\text{Bu}_4\text{N}_4)\text{Pd}^{\text{II}}\text{MeCl}$  (**4**) in 0.3 M  $\text{Bu}_4\text{NBF}_4/\text{CH}_2\text{Cl}_2$  at RT.

reduction appears at a potential  $\sim 600$  mV more negative compared to that of the anodic peak B (Figure 18 and Supporting Information, Figure S26). In addition, at higher scan rates ( $>5$  V/s) two additional irreversible waves appear at  $\sim 0.84$  and  $1.1$  V versus Fc, respectively (waves D and E, Figure 18). To assign the conformations responsible for these oxidation waves, we first compared the CVs of  $(\text{t}^{\text{Bu}}\text{N}4)\text{-Pd}^{\text{II}}\text{MeCl}$  and the product of its one-electron oxidation,  $[(\kappa^4\text{-t}^{\text{Bu}}\text{N}4)\text{Pd}^{\text{III}}\text{MeCl}](\text{BF}_4)$  ( $4^+[\text{BF}_4]$ ).<sup>44</sup> The tetradentate coordination of  $\text{t}^{\text{Bu}}\text{N}4$  in  $4^+$  was previously established by X-ray.<sup>44</sup> The CV of  $4^+[\text{BF}_4]$  in  $0.1$  M  $\text{Bu}_4\text{NBF}_4/\text{MeCN}$  exhibits a reversible anodic wave C ( $E_{1/2} = 584$  mV vs Fc,  $\Delta E_p = 69$ ) assigned to the  $\text{Pd}^{\text{III/IV}}$  redox couple of  $[(\kappa^4\text{-t}^{\text{Bu}}\text{N}4)\text{Pd}^{\text{III}}\text{MeCl}]^+$  and a cathodic wave A' ( $E_{pc} = -412$  mV vs Fc) assigned as the reduction of  $[(\kappa^4\text{-t}^{\text{Bu}}\text{N}4)\text{Pd}^{\text{III}}\text{MeCl}]^+$  to  $\text{Pd}^{\text{II}}$  (Figure 19b). By analogy, the peaks C and A' in the CV of **4** were also assigned to the  $\text{Pd}^{\text{III/IV}}$  oxidation and the  $\text{Pd}^{\text{III/II}}$  reduction for  $[(\kappa^4\text{-t}^{\text{Bu}}\text{N}4)\text{Pd}^{\text{III}}\text{MeCl}]^+$ , respectively.

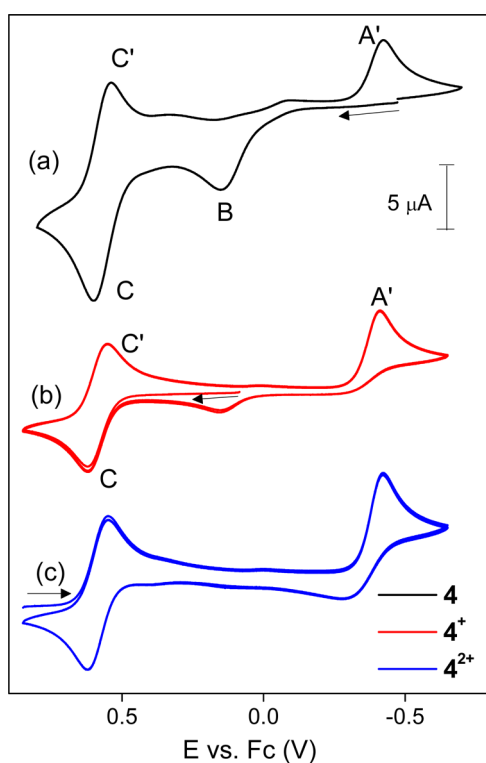


**Figure 19.** CVs of (a)  $(\text{t}^{\text{Bu}}\text{N}4)\text{Pd}^{\text{II}}\text{MeCl}$ , **4** (black line), (b)  $[(\text{t}^{\text{Bu}}\text{N}4)\text{Pd}^{\text{III}}\text{MeCl}](\text{BF}_4)$ ,  $4^+[\text{BF}_4]$  (red line; three cycles), and (c)  $[(\text{t}^{\text{Bu}}\text{N}4)\text{Pd}^{\text{IV}}\text{MeCl}](\text{BF}_4)_2$ ,  $4^{2+}[\text{BF}_4]_2$  (blue line; 3 cycles) in  $0.1$  M  $\text{Bu}_4\text{NBF}_4/\text{MeCN}$  ( $100$  mV/s, RT).

Given the large separation between the anodic wave B and the corresponding cathodic wave A' ( $\Delta E_p \approx 530$  mV), this redox process is most likely accompanied by a significant geometrical reorganization and a conformational change of  $\text{t}^{\text{Bu}}\text{N}4$ . Similarly to complexes **2** and **3**, the anodic wave C was assigned to the  $\text{Pd}^{\text{II/III}}$  oxidation of the  $(\kappa^3\text{-t}^{\text{Bu}}\text{N}4)\text{Pd}^{\text{II}}\text{MeCl}$  conformer. This assignment is also supported by the variable-temperature electrochemical studies described below.

The CV and DPV of **4** at  $-64$  °C exhibit two oxidation waves at high potentials,  $0.95$  and  $1.18$  V versus Fc (D and E, Figures 20 and 21). The first oxidation wave can be assigned to the  $\text{Pd}^{\text{II/III}}$  oxidation of the major conformer,  $(\kappa^2\text{-t}^{\text{Bu}}\text{N}4)\text{-Pd}^{\text{II}}\text{MeCl}$ .

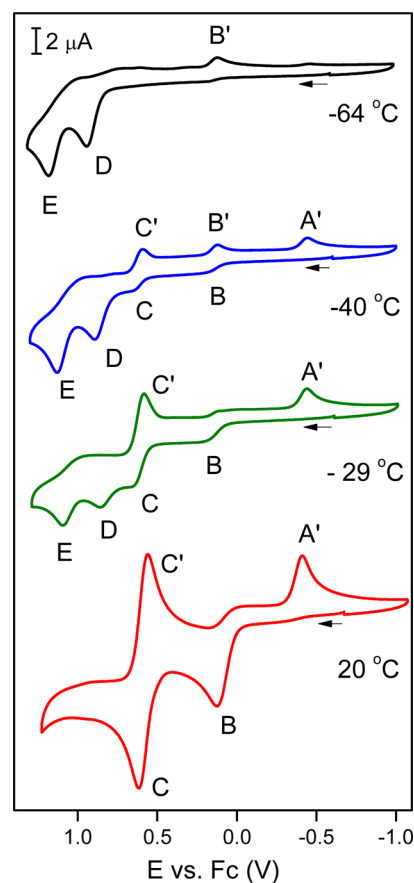


**Figure 20.** Variable-temperature CVs of  $(\text{t}^{\text{Bu}}\text{N}4)\text{Pd}^{\text{II}}\text{MeCl}$  (**4**) in  $0.3$  M  $\text{Bu}_4\text{NBF}_4/\text{CH}_2\text{Cl}_2$  ( $100$  mV/s).

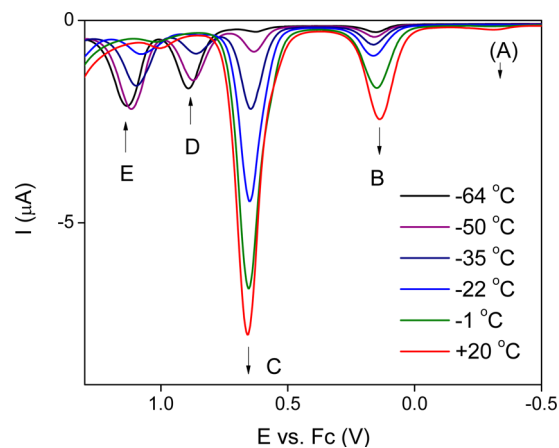


**Figure 21.** Variable-temperature DPV of  $(\text{t}^{\text{Bu}}\text{N}4)\text{Pd}^{\text{II}}\text{MeCl}$  (**4**) in  $0.3$  M  $\text{Bu}_4\text{NBF}_4/\text{CH}_2\text{Cl}_2$  (pulse amplitude  $0.05$  V). Arrows indicate the change of peak height when warming from  $-64$  to  $20$  °C.

$\text{Pd}^{\text{II}}\text{MeCl}$ . Interestingly, when the scan direction is reversed immediately after peak D, the cathodic scan reveals a reduction wave at a much more negative potential, B' (Supporting Information, Figure S33). The comparison with CVs recorded at higher temperatures (or at scan rates  $\geq 10$  V/s at RT) suggest that this reduction peak corresponds to the  $\text{Pd}^{\text{III/II}}$  reduction of the  $[(\kappa^3\text{-t}^{\text{Bu}}\text{N}4)\text{Pd}^{\text{III}}\text{MeCl}]^+$  conformer. Therefore, it is likely that oxidation of  $(\kappa^2\text{-t}^{\text{Bu}}\text{N}4)\text{Pd}^{\text{II}}\text{MeCl}$  produces a highly unstable  $[(\kappa^2\text{-t}^{\text{Bu}}\text{N}4)\text{Pd}^{\text{III}}\text{MeCl}]^+$  species, which quickly undergoes a geometric rearrangement to give the  $[(\kappa^3\text{-t}^{\text{Bu}}\text{N}4)\text{-Pd}^{\text{III}}\text{MeCl}]^+$ .

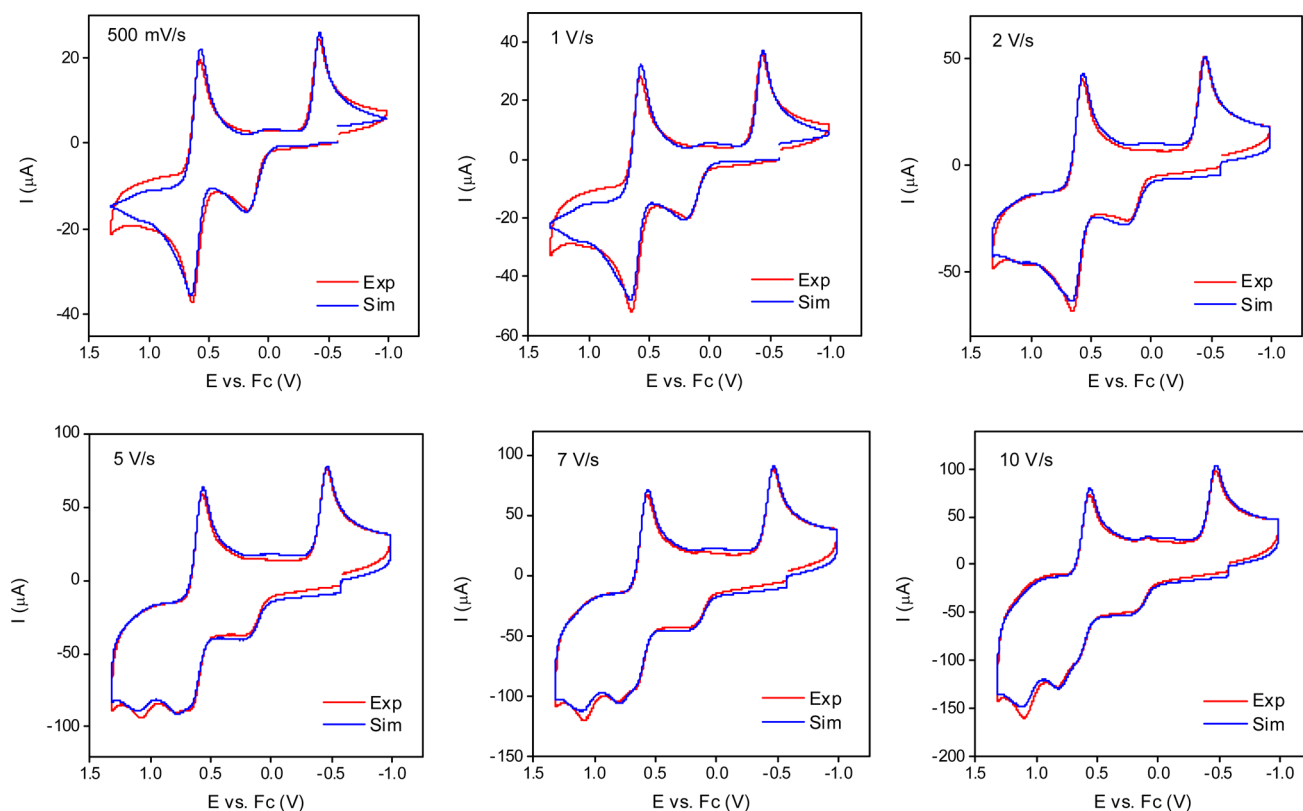


**Figure 22.** Experimental (red) and simulated (blue) CVs of 2.0 mM  $(\text{tBu}_4\text{N})\text{Pd}^{\text{II}}\text{MeCl}$  (**4**) in 0.1 M  $\text{Bu}_4\text{NBF}_4/\text{CH}_2\text{Cl}_2$  at various scan rates at RT.

$\text{Pd}^{\text{III}}\text{MeCl}]^+$  conformer that is observed at low temperatures during the reverse cathodic scan. Accordingly, the following irreversible oxidation wave E was assigned as the  $\text{Pd}^{\text{III/IV}}$  oxidation of  $[(\kappa^3\text{-tBu}_4\text{N})\text{Pd}^{\text{III}}\text{MeCl}]^+$ . Warming the solution of  $(\text{tBu}_4\text{N})\text{PdMeCl}$  leads to the appearance of the oxidation waves at lower potentials, B and C, that eventually become predominant at 20 °C, while waves D and E disappear (Figures 20 and 21). The oxidation wave B is quasi-reversible at -40 °C; however, at higher temperatures the reverse cathodic peak B' disappears due to rapid conformational change upon oxidation to the stable conformer  $[(\kappa^4\text{-tBu}_4\text{N})\text{Pd}^{\text{III}}\text{MeCl}]^+$ . Finally, the oxidation peak that would correspond to the  $\text{Pd}^{\text{II/III}}$  redox couple for  $(\kappa^4\text{-tBu}_4\text{N})\text{Pd}^{\text{II}}\text{MeCl}$  was not observed by CV even at slow scan rates, although a small peak was detected by DPV at 20 °C in the expected region (peak A in Figure 21). This suggests that if  $(\kappa^4\text{-tBu}_4\text{N})\text{Pd}^{\text{II}}\text{MeCl}$  indeed formed, it is present in very low concentrations.

The proposed electrochemical mechanism is strongly supported by the digital simulation of the variable scan rate CVs (Figure 22). A good agreement between the experimental data and the simulated CVs is obtained by employing the optimized simulation parameters given in Scheme 7. Together with the variable-temperature studies, these results suggest that the axial coordination of at least one amine donor occurs prior to oxidation to generate a more easily oxidized  $(\kappa^3\text{-tBu}_4\text{N})\text{-PdMeCl}$  conformer, and possibly even a  $(\kappa^4\text{-tBu}_4\text{N})\text{PdMeCl}$  species, suggestive of a CE mechanism. A nearly sigmoidal shape of the oxidation peak C at high scan rates ( $\geq 7$  V/s, Figures 18 and 22) or intermediate temperatures (-40 and -29 °C, Figure 20) is also suggestive of a CE mechanism.<sup>74</sup> Similar to complexes **3**<sup>+</sup> and **3a**<sup>+</sup>, the coordination of one axial amine donor in  $(\kappa^3\text{-tBu}_4\text{N})\text{Pd}^{\text{II}}\text{MeCl}$  lowers the  $\text{Pd}^{\text{II/III}}$  oxidation potential by ~600 mV compared to the major isomer

$(\kappa^2\text{-tBu}_4\text{N})\text{PdMeCl}$  (17 vs 617 mV, respectively, Scheme 7). Overall, this suggests that the minor isomer  $(\kappa^3\text{-tBu}_4\text{N})\text{-Pd}^{\text{II}}\text{MeCl}$ , and maybe even  $(\kappa^4\text{-tBu}_4\text{N})\text{Pd}^{\text{II}}\text{MeCl}$ , is likely responsible for the oxidation reactivity of **4** in organometallic reactions.<sup>44</sup>

Importantly, while it was reported previously on the basis of NMR studies that complex **4** exists as a single  $\kappa^2\text{-tBu}_4\text{N}$  conformer in solution, our electrochemical studies and digital CV simulations suggest that the  $\kappa^3\text{-tBu}_4\text{N}$  conformer may be present in a small amount, corresponding to a ratio of  $\kappa^2\text{-4}$  to  $\kappa^3\text{-4}$  conformers of ~10:1 ( $k_f/k_b = 10$  for the  $\kappa^2\text{-4}$  to  $\kappa^3\text{-4}$  interconversion). Thus, these CV simulations provide a semiquantitative description of the conformer ratio and support why the  $\kappa^3\text{-4}$  conformer was not observed in solution by NMR.<sup>52</sup> Overall, it is important to note that such electrochemical studies can provide additional insight into the various conformers responsible for the redox properties of these organometallic Pd complexes.

To investigate further the oxidation reactivity of **4**<sup>+</sup>, the controlled potential electrolysis of isolated  $[(\text{tBu}_4\text{N})\text{Pd}^{\text{III}}\text{MeCl}]^+$  was performed at 0.85 V versus Fc at -65 °C in 0.1 M  $\text{Bu}_4\text{NPF}_6/\text{EtCN}$  and monitored by UV-vis spectroscopy. During the electrolysis, the visible absorption band of the starting material at 723 nm disappears, and a red solution forms that is characterized by absorption bands at 486 nm ( $\epsilon = 2700 \text{ M}^{-1}\cdot\text{cm}^{-1}$ ) and 352 nm ( $\epsilon = 4800 \text{ M}^{-1}\cdot\text{cm}^{-1}$ , Figure 23). The product obtained after a one-electron oxidation is EPR silent, consistent with the formation of a  $\text{Pd}^{\text{IV}}$  species. The CV of the  $\text{Pd}^{\text{IV}}$  product (Figure 19c) is very similar to the CV of  $[(\text{tBu}_4\text{N})\text{Pd}^{\text{III}}\text{MeCl}]^+$  (Figure 19b) and exhibits a reversible  $\text{Pd}^{\text{IV/III}}$  reduction wave ( $E_{1/2} = 586 \text{ mV vs Fc}$ ,  $\Delta E_p = 71 \text{ mV}$ ) and an irreversible  $\text{Pd}^{\text{III/II}}$  reduction peak at -423 mV versus Fc. The equilibrium potential of **4**<sup>2+</sup> (682 mV vs Fc) is more

**Scheme 7. Mechanism Used for Simulation of Variable Scan Rate CVs of  $(^t\text{BuN4})\text{PdMeCl}$  (0.3 M  $\text{Bu}_4\text{NPF}_6/\text{CH}_2\text{Cl}_2$ , 298 K)<sup>a</sup>**

Electron transfer steps:	E (mV vs. Fc):	$k_e$ (cm/s):
$\kappa^3\text{-4}^{2+} + e^- \xrightleftharpoons[E]{E'} \kappa^3\text{-4}^+$	1017	0.005
$\kappa^2\text{-4}^+ + e^- \xrightleftharpoons[D]{D'} \kappa^2\text{-4}$	617	0.005
$\kappa^4\text{-4}^{2+} + e^- \xrightleftharpoons[C]{C'} \kappa^4\text{-4}^+$	601	1
$\kappa^3\text{-4}^+ + e^- \xrightleftharpoons[B]{B'} \kappa^3\text{-4}$	17	0.01
$\kappa^4\text{-4}^+ + e^- \xrightleftharpoons[A]{A'} \kappa^4\text{-4}$	-433	0.5
Chemical reactions:	$k_f$ (1/s):	$k_b$ (1/s):
$\kappa^2\text{-4} \xrightleftharpoons[k_b]{k_f} \kappa^3\text{-4}$	90	900
$\kappa^3\text{-4} \xrightleftharpoons[k_b]{k_f} \kappa^4\text{-4}$	16.4	1055
$\kappa^3\text{-4}^+ \xrightarrow{k_f} \kappa^4\text{-4}^+$	31.3	0
$\kappa^2\text{-4}^+ \xrightarrow{k_f} \kappa^3\text{-4}^+$	87.9	0
$\kappa^3\text{-4}^{2+} \xrightarrow{k_f} \kappa^4\text{-4}^{2+}$	30.8	0

<sup>a</sup>The experimental and simulated CVs are shown in Figure 21. Notation: 4 is  $[(^t\text{BuN4})\text{Pd}^{\text{II}}\text{MeCl}]^+$ , 4<sup>+</sup> is  $[(^t\text{BuN4})\text{Pd}^{\text{III}}\text{MeCl}]^+$ , and 4<sup>2+</sup> is  $[(^t\text{BuN4})\text{Pd}^{\text{IV}}\text{MeCl}]^{2+}$ .

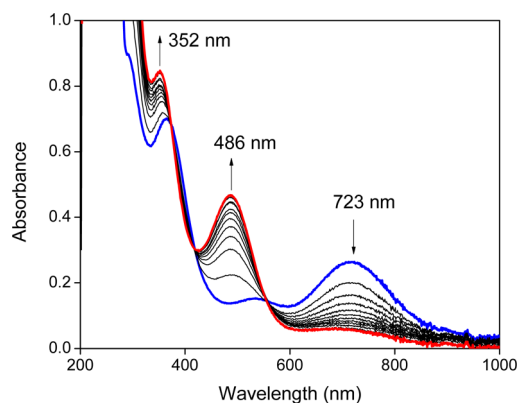


**Figure 23.** UV-vis spectra of electrooxidation of 1.8 mM  $[(^t\text{BuN4})\text{Pd}^{\text{III}}\text{MeCl}]^+$  (4<sup>+</sup>) in 0.1 M  $\text{Bu}_4\text{NPF}_6/\text{EtCN}$  (1 mm path length,  $-65^\circ\text{C}$ ,  $\Delta t = 15$  min). Arrows indicate the change of the absorption bands over time.

positive compared to the equilibrium potential of  $[(\text{N4})\text{Pd}^{\text{III}}\text{MeCl}]^+$  (85 mV vs Fc) and  $(^t\text{BuN4})\text{Pd}^{\text{II}}\text{MeCl}$  ( $-472$  mV vs Fc). A small separation between the anodic and cathodic peaks of the  $\text{Pd}^{\text{III/IV}}$  redox couple suggests that no significant structural changes occur during oxidation. Therefore, the product can be assigned as an octahedral  $[(\kappa^4\text{-}^t\text{BuN4})\text{Pd}^{\text{IV}}\text{MeCl}]^{2+}$  (4<sup>2+</sup>). Although the product was not isolated due to its limited stability, the X-ray analysis of the analogous complexes  $[(^R\text{N4})\text{Pd}^{\text{IV}}\text{MeCl}]^{2+}$  (R = Me, <sup>i</sup>Pr) established the

octahedral geometry around the  $\text{Pd}^{\text{IV}}$  center and the tetradentate coordination of  $^R\text{N4}$ .<sup>47</sup>

The marked similarity between the CVs of 4, 4<sup>+</sup>, and 4<sup>2+</sup> (Figure 19) suggests an excellent chemical reversibility of the interconversion between all three oxidation states. This is a unique feature of the  $(^R\text{N4})\text{Pd}$  (R = <sup>t</sup>Bu, <sup>i</sup>Pr, Me) systems enabled by the conformational and coordination flexibility of  $^R\text{N4}$  ligands that can support square planar  $\text{Pd}^{\text{II}}$  centers, as well as six-coordinate  $\text{Pd}^{\text{III}}$  and  $\text{Pd}^{\text{IV}}$  species.

**Electrochemical Oxidation Behavior of  $(^t\text{BuN4})\text{Pd}^{\text{II}}\text{Me}_2$  at Various Temperatures.** The complex  $(^t\text{BuN4})\text{Pd}^{\text{II}}\text{Me}_2$  (5) exists as a single conformer,  $(\kappa^2\text{-}^t\text{BuN4})\text{Pd}^{\text{II}}\text{Me}_2$ , in solution and in the solid state.<sup>44,45</sup> The CV of 5 at RT resembles that of 4 (Figure 24a).<sup>44,45</sup> By analogy to 4, the low-potential oxidation wave at  $-365$  mV versus Fc (peak B, Figure 24a) can be assigned as the  $\text{Pd}^{\text{II/III}}$  oxidation of the minor  $(\kappa^3\text{-}^t\text{BuN4})\text{Pd}^{\text{II}}\text{Me}_2$  conformer, followed by a reversible oxidation to  $\text{Pd}^{\text{IV}}$  of  $[(\kappa^4\text{-}^t\text{BuN4})\text{Pd}^{\text{III}}\text{Me}_2]^+$  ( $E_{1/2} = 41$  mV vs Fc, peaks C/C'). The cathodic wave A' observed during the reverse scan can be assigned as the  $\text{Pd}^{\text{III/II}}$  reduction for the  $[(\kappa^4\text{-}^t\text{BuN4})\text{Pd}^{\text{III}}\text{Me}_2]^+$  conformer. Similarly, the CV of the isolated  $[(\kappa^4\text{-}^t\text{BuN4})\text{Pd}^{\text{III}}\text{Me}_2]^+$  complex (Figure 24b) exhibits a reversible  $\text{Pd}^{\text{III/IV}}$  oxidation wave (peaks C/C') and the  $\text{Pd}^{\text{III/II}}$  reduction peak A' at similar potentials.<sup>44</sup>

By comparison, the CV of  $(^t\text{BuN4})\text{Pd}^{\text{II}}\text{Me}_2$  recorded in THF at  $-70^\circ\text{C}$  is markedly different and shows an irreversible wave at a much higher potential, 480 mV versus Fc (peak D, Figure 24c). The oxidation potential of  $(^t\text{BuN4})\text{Pd}^{\text{II}}\text{Me}_2$  at  $-70^\circ\text{C}$  is in fact similar to that reported for dimethyl complexes with bidentate N-donor ligands such as  $(^t\text{Bu}_2\text{bipy})\text{PdMe}_2$  (0.45 V. vs Fc).<sup>45,50</sup> By analogy to 4, the oxidation wave observed at  $-70^\circ\text{C}$  is likely due to the oxidation of the major conformer,  $(\kappa^2\text{-}^t\text{BuN4})\text{Pd}^{\text{II}}\text{Me}_2$ , as the isomerization to form  $(\kappa^3\text{-}^t\text{BuN4})\text{Pd}^{\text{II}}\text{Me}_2$  is slow at this temperature compared to the CV time scale. While more detailed electrochemical study of complex 5 could not be performed due to its limited stability in solution, it is expected that its conformational behavior will be similar to that of complex 4.

These results also suggest that the minor isomer  $(\kappa^3\text{-}^t\text{BuN4})\text{Pd}^{\text{II}}\text{Me}_2$  is most likely responsible for the unique aerobic reactivity of this complex, due to its dramatically lower  $\text{Pd}^{\text{II/III}}$  oxidation potential. For comparison, the analogous complexes with bidentate N-donor ligands such as  $(^t\text{Bu}_2\text{bipy})\text{Pd}^{\text{II}}\text{Me}_2$  are generally unreactive toward  $\text{O}_2$  in the absence of radical initiators. Therefore, irrespective of the most stable conformer in solution, use of conformationally flexible multidentate ligands that can provide axial donors to the metal center are ideally suited to promoting oxidation reactivity with mild oxidants such as  $\text{O}_2$ .

## CONCLUSION

In summary, we have explored in detail the redox properties of conformationally flexible  $(^t\text{BuN4})\text{Pd}^{\text{II}}$  complexes by employing variable scan rate and variable-temperature CV, DPV, and spectroelectrochemical studies, as well as digital CV simulations for a series of  $(^t\text{BuN4})\text{Pd}$  complexes that adopt various conformational states in solution ranging from  $(\kappa^2\text{-}^t\text{BuN4})\text{Pd}$  to  $(\kappa^3\text{-}^t\text{BuN4})\text{Pd}$  and  $(\kappa^4\text{-}^t\text{BuN4})\text{Pd}$ . We have also isolated and characterized several new  $\text{Pd}^{\text{III}}$  complexes including the monocationic  $[(^t\text{BuN4})\text{Pd}^{\text{III}}\text{Cl}_2]^+$  and the dicationic  $[(^t\text{BuN4})\text{Pd}^{\text{III}}\text{Me}(\text{MeCN})]^{2+}$  complexes that were characterized by X-ray analysis, as well as an unstable tricationic  $[(^t\text{BuN4})\text{Pd}^{\text{III}}(\text{EtCN})_2]^{3+}$  species characterized in solution by EPR and UV-vis spectroscopy.

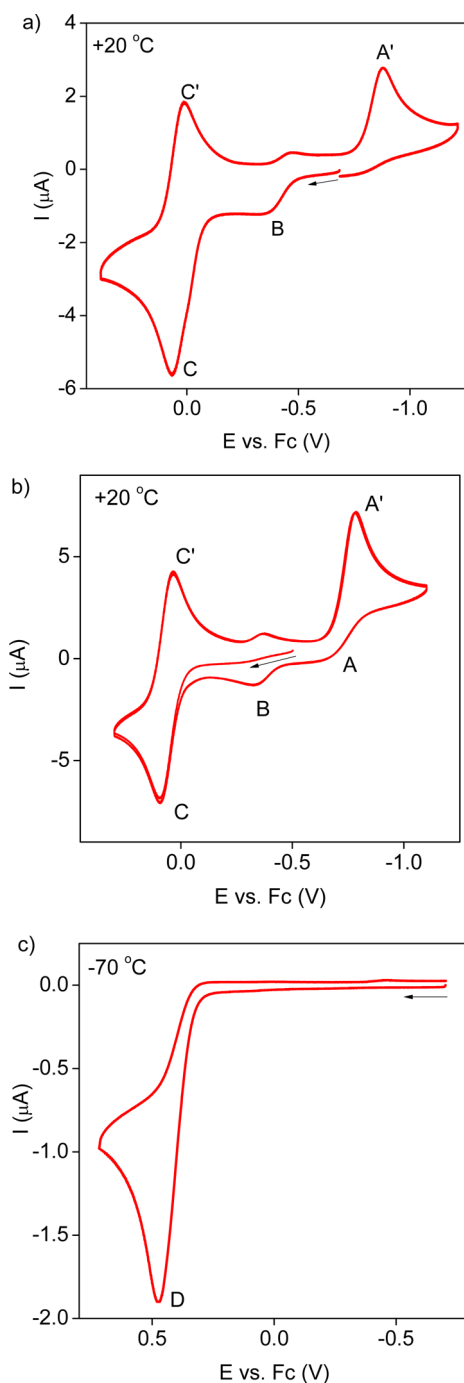


**Figure 24.** CVs of (a) 1 mM  $(\text{tBu}_4\text{N}_4)\text{Pd}^{\text{II}}\text{Me}_2$  (**5**) in 0.1 M  $\text{Bu}_4\text{NPF}_6/\text{THF}$  (100 mV/s), (b)  $[(\kappa^4\text{-tBu}_4\text{N}_4)\text{Pd}^{\text{III}}\text{Me}_2](\text{ClO}_4)$  in 0.3 M  $\text{Bu}_4\text{NPF}_6/\text{MeCN}$  (100 mV/s, 20 °C, 3 cycles), and (c) 2.7 mM  $(\text{tBu}_4\text{N}_4)\text{PdMe}_2$  (**5**) at  $-70$  °C (100 mV/s).

These electrochemical studies suggest that, irrespective of the most stable conformation(s) present in solution, the oxidation ability of these systems is determined by the minor, yet more easily oxidized conformer, in which one or two axial N-donors are interacting with the metal center. The formation of such  $(\kappa^3\text{-tBu}_4\text{N}_4)\text{Pd}$  or  $(\kappa^4\text{-tBu}_4\text{N}_4)\text{Pd}$  conformers occurs prior to oxidation through a ligand conformational change (i.e., a CE mechanism). A good agreement was obtained between the experimental and simulated CVs at variable scan rates, strongly supporting the proposed electrochemical mechanisms. Furthermore, the redox behavior of these conformationally flexible

complexes is highly temperature-dependent. At low temperatures, the electrochemical properties are determined by the most stable isomer, while at RT the rapid conformational changes generate conformers with lower oxidation potentials that determine the unique oxidation reactivity of these  $\text{Pd}^{\text{II}}$  complexes. The low-temperature studies also suggest that a tridentate  $\text{tBu}_4\text{N}_4$  may be sufficient to stabilize a  $\text{Pd}^{\text{III}}$  species, while a tetradentate  $\text{tBu}_4\text{N}_4$  is likely needed to access the  $\text{Pd}^{\text{IV}}$  species.

Overall, this study sheds light on the mechanism of redox transformations in Pd complexes with coordinatively flexible ligands and on the role of ligand conformations in determining the redox behavior of the Pd center. Importantly, we have determined that the presence of axial N-donors that can interact with the Pd center has a profound effect on the redox properties of the corresponding  $\text{Pd}^{\text{II}}$  complexes, and the coordination of each axial N-donor lowers the  $\text{Pd}^{\text{II/III}}$  oxidation potential by  $\sim 600$  mV, for a total of up to 1.2 V. Such dramatic lowering of the  $\text{Pd}^{\text{II/III}}$  oxidation potential is essential for the facile oxidation reactivity of these Pd systems. The conclusions drawn herein are relevant not only to  $\text{R}_4\text{N}_4$  complexes but also to other systems that involve conformationally flexible polydentate ligands.<sup>71,80,81</sup> These results are thus critical for designing new ligand systems that can promote Pd-catalyzed oxidation reactions employing mild oxidants.

## ■ ASSOCIATED CONTENT

### 📄 Supporting Information

Experimental methods, synthesis procedures, spectroscopic and electrochemical characterizations, and X-ray crystallographic data in CIF format. This material is available free of charge via the Internet at <http://pubs.acs.org>.

## ■ AUTHOR INFORMATION

### Corresponding Author

\*E-mail: [mirica@wustl.edu](mailto:mirica@wustl.edu).

### Present Address

<sup>§</sup>Okinawa Institute of Science and Technology Graduate University, 1919–1 Tancha, Onna-son, Kunigami-gun, Okinawa, Japan 904–0495.

### Notes

The authors declare no competing financial interest.

## ■ ACKNOWLEDGMENTS

We thank Prof. C. Nervi (University of Turin) and Prof. D. Gosser (CUNY) for providing the source codes for the programs ESP and CVSIM, respectively. We thank the American Chemical Society Petroleum Research Fund (No. 49914-DNI3) and the U.S. Department of Energy Catalysis Science Program (Grant No. DE-FG02-11ER16254) for support. L.M.M. is also supported by a Sloan Research Fellowship.

## ■ REFERENCES

- (1) Yamaguchi, J.; Yamaguchi, A. D.; Itami, K. *Angew. Chem., Int. Ed.* **2012**, *51*, 8960.
- (2) Rosen, B. R.; Simke, L. R.; Thuy-Boun, P. S.; Dixon, D. D.; Yu, J.-Q.; Baran, P. S. *Angew. Chem., Int. Ed.* **2013**, ASAP.
- (3) Lyons, T. W.; Sanford, M. S. *Chem. Rev.* **2010**, *110*, 1147.

- (4) Engle, K. M.; Mei, T. S.; Wang, X. S.; Yu, J. Q. *Angew. Chem., Int. Ed.* **2011**, *50*, 1478.
- (5) Engle, K. M.; Mei, T.-S.; Wasa, M.; Yu, J.-Q. *Acc. Chem. Res.* **2012**, *45*, 788.
- (6) Sehnal, P.; Taylor, R. J. K.; Fairlamb, I. J. S. *Chem. Rev.* **2010**, *110*, 824.
- (7) Muniz, K. *Angew. Chem., Int. Ed.* **2009**, *48*, 9412.
- (8) Xu, L.-M.; Li, B.-J.; Yang, Z.; Shi, Z.-J. *Chem. Soc. Rev.* **2010**, *39*, 712.
- (9) Kalyani, D.; Dick, A. R.; Anani, W. Q.; Sanford, M. S. *Tetrahedron* **2006**, *62*, 11483.
- (10) Racowski, J. M.; Sanford, M. S. *Top. Organomet. Chem.* **2011**, *35*, 61.
- (11) Canty, A. J. *Acc. Chem. Res.* **1992**, *25*, 83.
- (12) Deprez, N. R.; Sanford, M. S. *Inorg. Chem.* **2007**, *46*, 1924.
- (13) Luinstra, G. A.; Wang, L.; Stahl, S. S.; Labinger, J. A.; Bercaw, J. E. *J. Organomet. Chem.* **1995**, *504*, 75.
- (14) Shilov, A. E.; Shul'pin, G. B. *Chem. Rev.* **1997**, *97*, 2879.
- (15) Engle, K. M.; Yu, J.-Q. *J. Org. Chem.* **2013**, ASAP.
- (16) Giri, R.; Lan, Y.; Liu, P.; Houk, K. N.; Yu, J.-Q. *J. Am. Chem. Soc.* **2012**, *134*, 14118.
- (17) Stowers, K. J.; Kubota, A.; Sanford, M. S. *Chem. Sci.* **2012**, *3*, 3192.
- (18) Emmert, M. H.; Cook, A. K.; Xie, Y. J.; Sanford, M. S. *Angew. Chem., Int. Ed.* **2011**, *50*, 9409.
- (19) Bar-Nahum, I.; Khenkin, A. M.; Neumann, R. *J. Am. Chem. Soc.* **2004**, *126*, 10236.
- (20) Vedernikov, A. N. *Acc. Chem. Res.* **2012**, *45*, 803.
- (21) Campbell, A. N.; Stahl, S. S. *Acc. Chem. Res.* **2012**, *45*, 851.
- (22) McAuley, A.; Whitcombe, T. W. *Inorg. Chem.* **1988**, *27*, 3090.
- (23) Khusnutdinova, J. R.; Rath, N. P.; Mirica, L. M. *Angew. Chem., Int. Ed.* **2011**, *50*, 5532.
- (24) Khusnutdinova, J. R.; Qu, F.; Zhang, Y.; Rath, N. P.; Mirica, L. M. *Organometallics* **2012**, *31*, 4627.
- (25) Qu, F.; Khusnutdinova, J. R.; Rath, N. P.; Mirica, L. M. *Chem. Commun.* **2014**, *50*, 3036.
- (26) Zhang, J.; Khaskin, E.; Anderson, N. P.; Zavalij, P. Y.; Vedernikov, A. N. *Chem. Commun.* **2008**, 3625.
- (27) Khusnutdinova, J. R.; Newman, L. L.; Vedernikov, A. N. *J. Organomet. Chem.* **2011**, *696*, 3998.
- (28) Sarneski, J. E.; McPhail, A. T.; Onan, K. D.; Erickson, L. E.; Reilly, C. N. *J. Am. Chem. Soc.* **1977**, *99*, 7376.
- (29) Wiegardt, K.; Koeppen, M.; Swiridoff, W.; Weiss, J. J. *Chem. Soc., Dalton Trans.* **1983**, 1869.
- (30) Davies, M. S.; Hambley, T. W. *Inorg. Chem.* **1998**, *37*, 5408.
- (31) Prokopchuk, E. M.; Jenkins, H. A.; Puddephatt, R. J. *Organometallics* **1999**, *18*, 2861.
- (32) Prokopchuk, E. M.; Puddephatt, R. J. *Can. J. Chem.* **2003**, *81*, 476.
- (33) Vedernikov, A. N.; Binfield, S. A.; Zavalij, P. Y.; Khusnutdinova, J. R. *J. Am. Chem. Soc.* **2006**, *128*, 82.
- (34) Blake, A. J.; Holder, A. J.; Hyde, T. I.; Schröder, M. *J. Chem. Soc., Chem. Commun.* **1987**, 987.
- (35) Blake, A. J.; Gordon, L. M.; Holder, A. J.; Hyde, T. I.; Reid, G.; Schröder, M. *J. Chem. Soc., Chem. Commun.* **1988**, 1452.
- (36) Reid, G.; Blake, A. J.; Hyde, T. I.; Schröder, M. *J. Chem. Soc., Chem. Commun.* **1988**, 1397.
- (37) Hunter, G.; McAuley, A.; Whitcombe, T. W. *Inorg. Chem.* **1988**, *27*, 2634.
- (38) Blake, A. J.; Reid, G.; Schröder, M. *J. Chem. Soc., Dalton Trans.* **1990**, 3363.
- (39) Blake, A. J.; Crofts, R. D.; De Groot, B.; Schröder, M. *J. Chem. Soc., Dalton Trans.* **1993**, 485.
- (40) Stephen, E.; Blake, A. J.; Carter, E.; Collison, D.; Davies, E. S.; Edge, R.; Lewis, W.; Murphy, D. M.; Wilson, C.; Gould, R. O.; Holder, A. J.; McMaster, J.; Schröder, M. *Inorg. Chem.* **2012**, *51*, 1450.
- (41) Rostovtsev, V. V.; Henling, L. M.; Labinger, J. A.; Bercaw, J. E. *Inorg. Chem.* **2002**, *41*, 3608.
- (42) Chuang, G. J.; Wang, W.; Lee, E.; Ritter, T. *J. Am. Chem. Soc.* **2011**, *133*, 1760.
- (43) Kalyani, D.; McMurtrey, K. B.; Neufeldt, S. R.; Sanford, M. S. *J. Am. Chem. Soc.* **2011**, *133*, 18566.
- (44) Khusnutdinova, J. R.; Rath, N. P.; Mirica, L. M. *J. Am. Chem. Soc.* **2010**, *132*, 7303.
- (45) Khusnutdinova, J. R.; Rath, N. P.; Mirica, L. M. *J. Am. Chem. Soc.* **2012**, *134*, 2414.
- (46) Tang, F.; Zhang, Y.; Rath, N. P.; Mirica, L. M. *Organometallics* **2012**, *31*, 6690.
- (47) Tang, F.; Qu, F.; Khusnutdinova, J. R.; Rath, N. P.; Mirica, L. M. *Dalton Trans.* **2012**, *41*, 14046.
- (48) Khusnutdinova, J. R.; Mirica, L. M. In *C-H and C-X Bond Functionalization: Transition Metal Mediation*; Ribas, X., Ed.; Royal Society of Chemistry: Cambridge, U.K., 2013; p 122.
- (49) Mirica, L. M.; Khusnutdinova, J. R. *Coord. Chem. Rev.* **2013**, *257*, 299.
- (50) Lanci, M. P.; Remy, M. S.; Kaminsky, W.; Mayer, J. M.; Sanford, M. S. *J. Am. Chem. Soc.* **2009**, *131*, 15618.
- (51) Che, C. M.; Li, Z. Y.; Wong, K. Y.; Poon, C. K.; Mak, T. C. W.; Peng, S. M. *Polyhedron* **1994**, *13*, 771.
- (52) Meneghetti, S. P.; Lutz, P. J.; Kress, J. *Organometallics* **2001**, *20*, 5050.
- (53) Shen, H.; Jordan, R. F. *Organometallics* **2003**, *22*, 1878.
- (54) De Graaf, W.; Boersma, J.; Smeets, W. J. J.; Spek, A. L.; Van Koten, G. *Organometallics* **1989**, *8*, 2907.
- (55) Gottlieb, H. E.; Kotlyar, V.; Nudelman, A. *J. Org. Chem.* **1997**, *62*, 7512.
- (56) ESP was provided by Prof. C. Nervi (University of Turin) and is available at [http://lem.ch.unito.it/chemistry/esp\\_manual.html](http://lem.ch.unito.it/chemistry/esp_manual.html).
- (57) Zanello, P.; Nervi, C.; De Biani, F. F. *Inorganic Electrochemistry: Theory, Practice and Application*; Royal Society of Chemistry: Cambridge, U.K., 2012.
- (58) Gosser, D. K., Jr.; Zhang, F. *Talanta* **1991**, *38*, 715.
- (59) Gosser, D. K. *Cyclic Voltammetry: Simulation and Analysis of Reaction Mechanisms*; VCH: Weinheim, Germany, 1993.
- (60) *Apex II and SAINT*; Bruker AXS: Madison, WI, 2008.
- (61) Sheldrick, G. M. *Acta Crystallogr.* **2008**, *A64*, 112.
- (62) Khusnutdinova, J. R.; Luo, J.; Rath, N. P.; Mirica, L. M. *Inorg. Chem.* **2013**, *52*, 3920.
- (63) Koch, W. O.; Krüger, H.-J. *Angew. Chem., Int. Ed.* **1995**, *34*, 2671.
- (64) Graf, M.; Wolmershäuser, G.; Kelm, H.; Demeschko, S.; Meyer, F.; Krüger, H.-J. *Angew. Chem., Int. Ed.* **2010**, *49*, 950.
- (65) Koch, W. O.; Schünemann, V.; Gerdan, M.; Trautwein, A. X.; Krüger, H.-J. *Chem.—Eur. J.* **1998**, *4*, 686.
- (66) Kelm, H.; Krüger, H.-J. *Inorg. Chem.* **1996**, *35*, 3533.
- (67) Meneghetti, S. P.; Lutz, P. J.; Fischer, J.; Kress, J. *Polyhedron* **2001**, *20*, 2705.
- (68) Chandrasekhar, S.; McAuley, A. *Inorg. Chem.* **1992**, *31*, 2663.
- (69) Grant, G. J.; Sanders, K. A.; Setzer, W. N.; VanDerveer, D. G. *Inorg. Chem.* **1991**, *30*, 4053.
- (70) Blake, A. J.; Holder, A. J.; Hyde, T. I.; Roberts, Y. V.; Lavery, A. J.; Schröder, M. *J. Organomet. Chem.* **1987**, *323*, 261.
- (71) Grant, G. J.; Spangler, N. J.; Setzer, W. N.; VanDerveer, D. G.; Mehne, L. F. *Inorg. Chim. Acta* **1996**, *246*, 31.
- (72) Blake, A. J.; Holder, A. J.; Roberts, Y. V.; Schröder, M. *J. Chem. Soc., Chem. Commun.* **1993**, 260.
- (73) See Supporting Information.
- (74) Zanello, P. *Inorganic Electrochemistry. Theory, Practice and Application*; RSC: Cambridge, U.K., 2003.
- (75) Geiger, W. E. In *Progress in Inorganic Chemistry*; John Wiley & Sons, Inc.: Hoboken, NJ, 1985; p 275.
- (76) Liu, T.; Chen, S.; O'Hagan, M. J.; Rakowski DuBois, M.; Bullock, R. M.; DuBois, D. L. *J. Am. Chem. Soc.* **2012**, *134*, 6257.
- (77) O'Hagan, M.; Shaw, W. J.; Raugai, S.; Chen, S.; Yang, J. Y.; Kilgore, U. J.; DuBois, D. L.; Bullock, R. M. *J. Am. Chem. Soc.* **2011**, *133*, 14301.

- (78) Vedernikov, A. N.; Pink, M.; Caulton, K. G. *Inorg. Chem.* **2004**, *43*, 3642.
- (79) Vedernikov, A. N. *Chem. Commun.* **2009**, 4781.
- (80) Durrant, M. C.; Fairhurst, S. A.; Hughes, D. L.; Ibrahim, S. K.; Passos, M.; Pickett, C. J.; Queiros, A.; Queiros, A. *Chem. Commun.* **1997**, 2379.
- (81) Hunter, G.; McAuley, A.; Whitcombe, T. W. *Inorg. Chem.* **1988**, *27*, 2634.